Hyperspectral reflectance of pristine, ocean weathered and biofouled plastics from dry to wet and submerged state

Robin V. F. de Vries [1], Shungudzemwoyo P. Garaba [1, 2], Sarah-Jeanne Royer [1, 3]

[1] The Ocean Cleanup, Batavierenstraat 15, 3014 JH Rotterdam, The Netherlands

[2] Institute for Chemistry and Biology of the Marine Environment, Carl von Ossietzky University of Oldenburg, Schleusenstraße 1, Wilhelmshaven 26382, Germany

[3] Hawaiʻi Pacific University, The Center for Marine Debris Research, Hawaiʻi, USA

Correspondence to: Robin de Vries (robin.devries@theoceancleanup.com)

Abstract

High-quality spectral reference libraries are important for algorithm development and identification of diagnostic optical features of target objects in environmental remote sensing applications. We present additional measurements conducted using hyperspectral sensor technologies in a laboratory and outdoor setting to further extend high-quality data as well as diversity in available open-access spectral reference libraries. These observations involved gathering hyperspectral single-pixel point and multi-pixel optical properties of a diverse set of plastic materials (e.g., ropes, nets, packaging, and personal protective equipment). Measurements of COVID-19 personal protective equipment were conducted to also further expand reference datasets that could be useful in monitoring mismanaged waste related to the pandemic. The sample set consisted of virgin polymers and ocean-weathered and artificially biofouled objects of varying apparent colors, shapes, forms, thicknesses, and opacity. A Spectral Evolution spectroradiometer was used to collect hyperspectral reflectance single pixel point information from 280 – 2500 nm. Imaging was also performed using a Specim IQ hyperspectral camera from 400 – 1000 nm. Sampling underwater was completed in intervals of 0.005 m to 0.215 m within a 0.005 - 0.715 m depth range. All optical measurements are available in open-access for the laboratory experiment through https://doi.org/10.4121/769cc482-b104-4927-a94b-b16f6618c3b3 (de Vries and Garaba, 2023) and outdoors campaign involving the biofouling samples via https://doi.org/10.4121/7c53b72a-be97-478b-9288-ff9c850de64b (de Vries et al., 2023).

1   Introduction

Aquatic plastic waste is a threat to the socioeconomics and health state of the blue planet (Barboza et al., 2018; Beaumont et al., 2019; UNEP, 2021). Therefore, it is essential to have an interdisciplinary strategy for understanding the challenges and complexities related to global pollution by plastic waste. Among key approaches of scientific evidence-based research, remote sensing has emerged as a potential tool that could support monitoring the sources and sinks of this aquatic plastic waste (Maximenko et al., 2019; Van Sebille et al., 2020; Martínez-Vicente et al., 2019). The potential application of remote sensing technologies is ongoing, and promising findings have been reported from laboratory or mesocosm (Goddijn-Murphy and

Dufaur, 2018; Garaba et al., 2021), ship (de Vries et al., 2021), aircraft (Garaba et al., 2018), satellite-based studies (Park et al., 2021; Topouzelis et al., 2019), and sensitivity analyses that combine laboratory measurements incomplete radiative transfer computations to top of the atmosphere (Garaba and Harmel, 2022).

35 At present, optical-based remote sensing methodologies gather multi- or hyperspectral radiometric quantities to investigate and determine diagnostic reflectance characteristics of plastic waste. The unique optical features in the visible to longwave infrared spectrum are essential as they help develop algorithms for detecting or distinguishing plastics from other optically active components of the natural environment (Garaba et al., 2020; Tasseron et al., 2021a; Guffogg et al., 2021). Furthermore, collecting diverse measurements is important in further expanding open-access spectral reference libraries considering the

40 variability of optically active materials in the natural environment. Such diverse and extensive spectral reference libraries composed of well-curated end-member information are invaluable. They can be used to match unknown spectra with known materials using statistical metrics that evaluate the similarity in signal shape of the observed samples. Beyond spectral matching techniques, depth-related spectral reflectance datasets may lead to methods for detecting physical characteristics such as the buoyancy and subsequently windage of plastic litter. To this end, there are ongoing efforts to produce high-quality open-access

45 spectral reference libraries and fill the scientific data gaps (**Table 1**).

Among recent studies in **Table 1**, (Leone et al., 2023; Knaeps et al., 2021) have examined submerged plastics in depths of up to 0.08 m and 0.32 m, respectively. Because plastic litter in the open ocean frequently occurs in the water column down to 5 m depth (Kooi et al., 2016; Law et al., 2014), it remains relevant to extend remote sensing research to larger water depths

50 beyond existing datasets. By including measurements of up to 0.715 m water depth, this study aims to expand knowledge of spectral reflectance of deeply submerged plastic litter, simultaneously adding a finer resolution of depth. The study of (Leone et al., 2023) was conducted in parallel with this study, and the pristine plastic samples used there were created and provided by the authors of this study to enable cross-comparison between datasets. Parallel measurement campaigns with identical samples can assist other researchers in the comparison of setups and bring valuable insights into the implications of study and

55 instrumentation design.

In this study, we describe a dataset that further adds to existing open-access research by (i) increasing the depth resolution, including ranges at which submerged plastics were investigated, (ii) assessing the optical characteristics of active or freshly biofouled plastic samples, (iii) investigating reflectance properties using artificial laboratory-based as well as natural light in

60 outdoor settings, (iv) sampling a diverse set of materials ranging from pristine, ocean weathered to personal protective equipment and (v) using a synergy of advanced technologies from imaging to point measurement tasks. The metadata attached to the measurements obtained in our study is anticipated to be of additional value in radiative transfer simulations aimed at understanding how remote sensing efforts could be affected by biofouling and the submersion of polymers.

65   **Table 1:** Comparison of open-access spectral reference libraries containing plastic materials.

Study	Scenarios	Water Depth Intervals	Depth Range (m)	Quantified sample thickness	Biofouling	Wavelength Range (nm)	Polymer Types	Water type, lighting
This dataset	Dry and Wet Submersion Biofouling	21▲, 4•	0–0.70	yes	Active Mesocosm Wet	280 – 2500▲, 400 – 1000•	PS, HDPE, PP, PET-G, PVC, XPS, PA6-XT, Other, Unknown	Freshwater, indoor and outdoor combined
(Leone et al., 2023)	Dry and Wet Submersion Water Clarity Biofouling	4▲	0 – 0.08	yes	Mesocosm	350 – 2500▲	PE, PP, PET, PETa, PETc, PS, PVC, HDPE, LDPE, XPS, PA6, TPe, Fluorocarbon	Freshwater, indoor
(Knaeps et al., 2021)	Dry and Wet Submersion Water Clarity	7▲	0 – 0.32	no	Natural Dry	350 – 2500▲, 280 – 2500▲	PET, LDPE, PP, Polyester, Uknown	Freshwater, indoor
(Garaba et al., 2021)	Dry and Wet Pixel Coverage Geometry	1▲	–	no	Natural Dry	350 – 2500▲	LDPE, HDPE, PP, PS, Unknown	Freshwater, indoor and outdoor
(Tasseron et al., 2021b)	Dry and Wet	1•	–	no	Natural Dry	400 – 1000•, 1000 – 1700•	LDPE, HDPE, PS, PP, PET, PO	Freshwater, indoor
(Garaba et al., 2020)	Dry	1▲	–	no	Natural Dry	6000 – 14000▲	PET, PS, Unspecified	Not applicable, indoor
(Garaba and Dierssen, 2020)	Pellets and microplastic	1▲	–	no	–	350 – 2500▲	PVC, PA6, PA6.6, LDPE, PET, PP, PS, FEP, ABS, Merlon, PMMA	Not applicable, outdoor

• imaging and ▲ point measurements. * indicates variation in sample thickness related to pristine samples. ABS: terpolymer lustran 752; FEP: fluorinated ethylene propylene Teflon; LDPE: low-density polyethylene; HDPE: high-density polyethylene; PA6: polyamide 6; PA6.6: polyamide 66; PE: polyethylene; PET: polyethylene terephthalate; PETa: polyethylene terephthalate amorphous; PETc: polyethylene

terephthalate crystalline; PET-G: polyethylene terephthalate glycol; PMMA: polymethyl methacrylate; PO: polyolefin; PP: polypropylene; PS: polystyrene; PVC: polyvinyl chloride; and TPe: Thermoplastic elastomers.

2 Methods and materials

2.1 Indoor laboratory experiment

2.1.1 Samples

A set of pristine plastics was selected as standard reference samples (**Figure A1** and **Table 2**). The pristine samples included high-density polyethylene (HDPE), polypropylene (PP), polyvinylchloride (PVC), polyamide 6 (PA6), polyethylene terephthalate glycol (PET-G), and expanded polystyrene (XPS). The thickness of these pristine samples was 1 mm, 5 mm, and 10 mm for all materials. The polymer materials were chosen based on occurrence in rivers and oceans, e.g. (Lebreton et al., 2018; GESAMP, 2019). These pristine samples had a fixed length and width of 0.3 m by 0.3 m and were sourced from Steon Engineering Plastics in Rotterdam, The Netherlands. The XPS styrodur, by exception, was obtained from Van Beek Art Supplies in The Netherlands.

Weathered fishing nets, blue, and white fragments harvested by The Ocean Cleanup System 001/B from the Great Pacific Garbage Patch (GPGP) in 2019 were included in the sample set for this study (**Figure A1** and **Table 2**). A multilayer packaging bag was also included as weathered household waste.

The amount of waste associated with the COVID-19 pandemic was also considered relevant because the number of single-use items that were likely mismanaged could end up in the natural environment (Benson et al., 2021). The common single-use personal protective equipment was considered to be blue surgical gloves, surgical masks, and rapid antigen tests (**Figure A1** and Table 2).

Table 2 Overview of pristine (1 – 6) and harvested/weathered (7 – 16) samples. All pristine materials were square plates measuring 0.3 m x 0.3 m. The other materials were irregular in shape but made large enough to ensure 100% pixel coverage for the spectroradiometer.

ID	Polymer	Condition/Appearance	Thickness (mm)
01	HDPE	Pristine plastic	1, 5, 10
02	PP	Pristine plastic	1, 5, 10
03	PVC	Pristine plastic	1, 5, 10
04	PET-G	Pristine plastic	1, 5, 10
05	PA6-XT	Pristine plastic	1, 5, 10
06	PS (XPS Styrodur anthracite)	Pristine plastic	1, 5, 10
07	PP (oceanic)	White weathered, biofouled, top	*~ 3*

08	PP (oceanic)	White weathered, biofouled, bottom	~ 3
09	HDPE (oceanic)	Blue, weathered, biofouled	~ 1 - 3
10	HDPE (oceanic)	Green Net	Mesh of 2 mm twines
11	HDPE (oceanic)	White/Gray Rope	~5
12	Multilayer Packaging	Coffee bean package outside	<1
13	Multilayer packaging	Coffee bean package inside	<1
14	PS	Blue/green foam, used	20
15	HDPE fabric + LDPE coating	White construction sail	< 1
16	HDPE fabric + LDPE coating	Green construction sail	< 1
17	HDPE fabric + LDPE coating	Brown construction sail	< 1
18	Unknown	Medical: Rapid Antigen tests, Top	~ 5
19	Unknown	Medical: Rapid Antigen tests, Bottom	~ 5
20	Unknown	Medical: Gloves, New	< 1
21	Unknown	Medical: Gloves, Weathered	< 1
22	Unknown	Medical: Facemasks, New	< 1
23	Unknown	Medical: Facemasks, Weathered	< 1

2.1.2 Experimental setup

Single pixel point measurements were completed using a hyperspectral Spectral Evolution SR-3501 (SEV) spectroradiometer from the Ultraviolet (UV, 280 nm) to Shortwave Infrared (SWIR, 2500 nm) with an 8° field-of-view lens attached. The sensor illuminates a circular swath, centered in the middle of the sample, with a growing diameter dependent on the sample submergence depth. The swath width is calculated using **Equation 1,** where h is the sensor-to-sample distance. Here the fixed sensor-to-water distance was 0.398 m. Optical refraction effects in the water-air interface were presumed negligible because all observations were made from the nadir at a 0° viewing angle and in calm water conditions. The maximum swath size was reached at the 0.715 m depth mark, where it reaches a diameter of 0.156 m.

$$r_0 = h \cdot \tan\left(\frac{\alpha}{2}\right) \tag{1}$$

Relative reflectance was automatically determined at interpolated 1 nm spectral resolution by white referencing using a SphereOptics Zenith Polymer® SG3120 ≈ 99 % full material PTFE standard panel, in line with recent studies (Knaeps et al., 2021; Leone et al., 2023; Garaba et al., 2021). To minimize inconsistencies in light intensity, related to the use of indoor scattered light sources, the white reference panel was positioned at the surface level position, as close as possible to the sample position. Since the main focus of this study is on relative changes in the spectral reflectance curve shape, any potential further imperfections in light intensity were accepted in exchange for the benefits of an indoor laboratory environment, which include stability of lighting and the absence of adverse weather influences. Each measurement is an average of 20 raw scans. Reference true colour images were obtained using a Nikon Coolpix W300 16 MP digital camera for each sample, except for the six

110 homogeneous pristine plastic samples. Figure 1**Error! Reference source not found.** shows the indoor laboratory setup (design and as-built impression).

From a subset of irregular materials, we additionally collected hyperspectral imagery using a SPECIM IQ CMOS hyperspectral camera covering a wavelength range of 400 nm to 1000 nm with a spectral resolution of 7 nm. The camera has a 40 ° field-of-

115 view with a 1.3 MP focus and a 5 MP viewfinder camera. SPECIM IQ imaging was done remotely using a USB connection to obtain real-time true colour images and initiate hyperspectral imaging via the SPECIM IQ Studio version 2019.05.29.2 software. White referencing to determine relative reflectance was completed using a standard white panel supplied by SPECIM IQ. Figure 2 shows the setup (a) and the samples (b) for which SPECIM hypercubes were collected, where the viewfinder image is shown adjacent to the RGB composite from the hypercubes.

120 ### 2.1.3   Sample fixation and submergence

As illustrated in Figure 1, an aluminum pipe connected the sample holder to the main frame, allowing depth adjustments by unclamping, moving, and clamping the cylinder. The structure also provided movable mounting points for the spectroradiometer and imaging sensors. The frame itself could move along two rails on top of the tank. MOTIP black primer was sprayed on the frame part to mitigate background or stray light. The target area was illuminated by two ARRI Arrilite 750

125 Plus 575 W HPL halogen tungsten lamps set at 1.80 m above the ground directed at ~45 ° off the nadir on both sides of the tank. A 0.3 m x 0.3 m sample holder fixed the samples at progressive depths. To prevent sample buckling and consequent irregularities in the depth measurement, thin samples were further fixed by a glass window on top. All samples were supported by a 0.3 x 0.3 x 0.05 m black aluminum plate. The black aluminum plate was first abrased by 300-grain sandpaper, cleaned, degreased, and painted with a base layer of MOTIP EAN 8711347206407 black primer, then two layers of the blackest acrylic

130 paint in the world, Black 3.0. The tank was filled with fresh water.
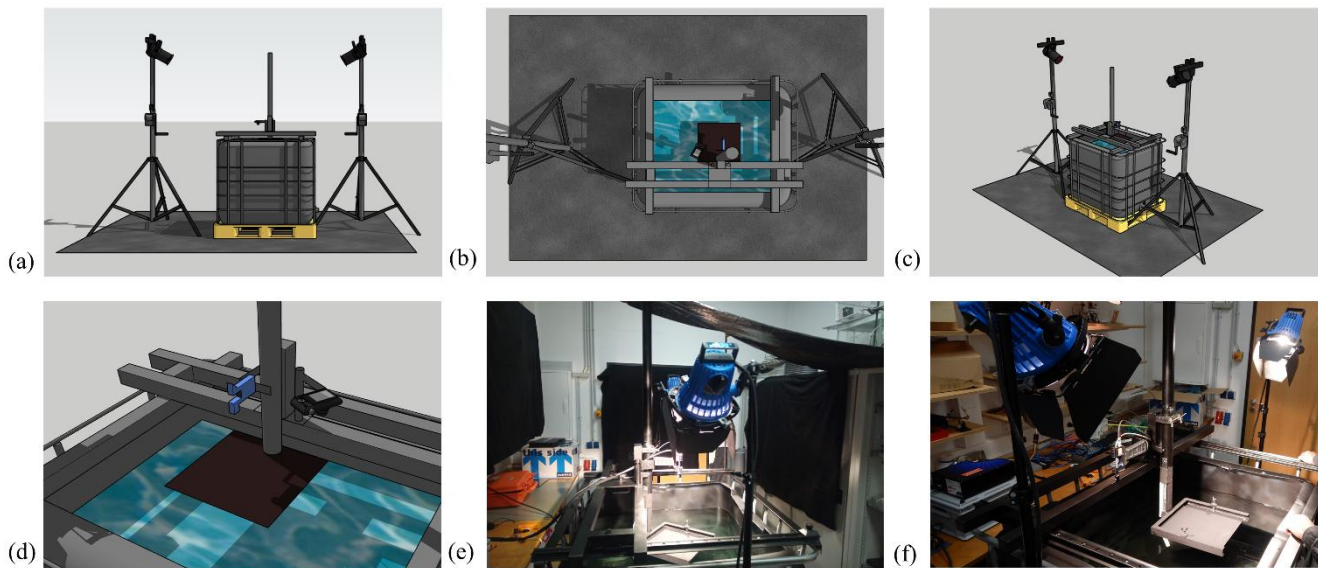
Figure 1 (a-d) Schematics and (c-d) true colour photos of the laboratory-based experimental setup with a dark container used to store the fresh water for submerged reflectance measurements. Background walls and frames were covered with dark fabric to mitigate stray light. Halogen tungsten lamps were used to provide artificial lighting above the tank at a ~45 ° nadir viewing angle.

135
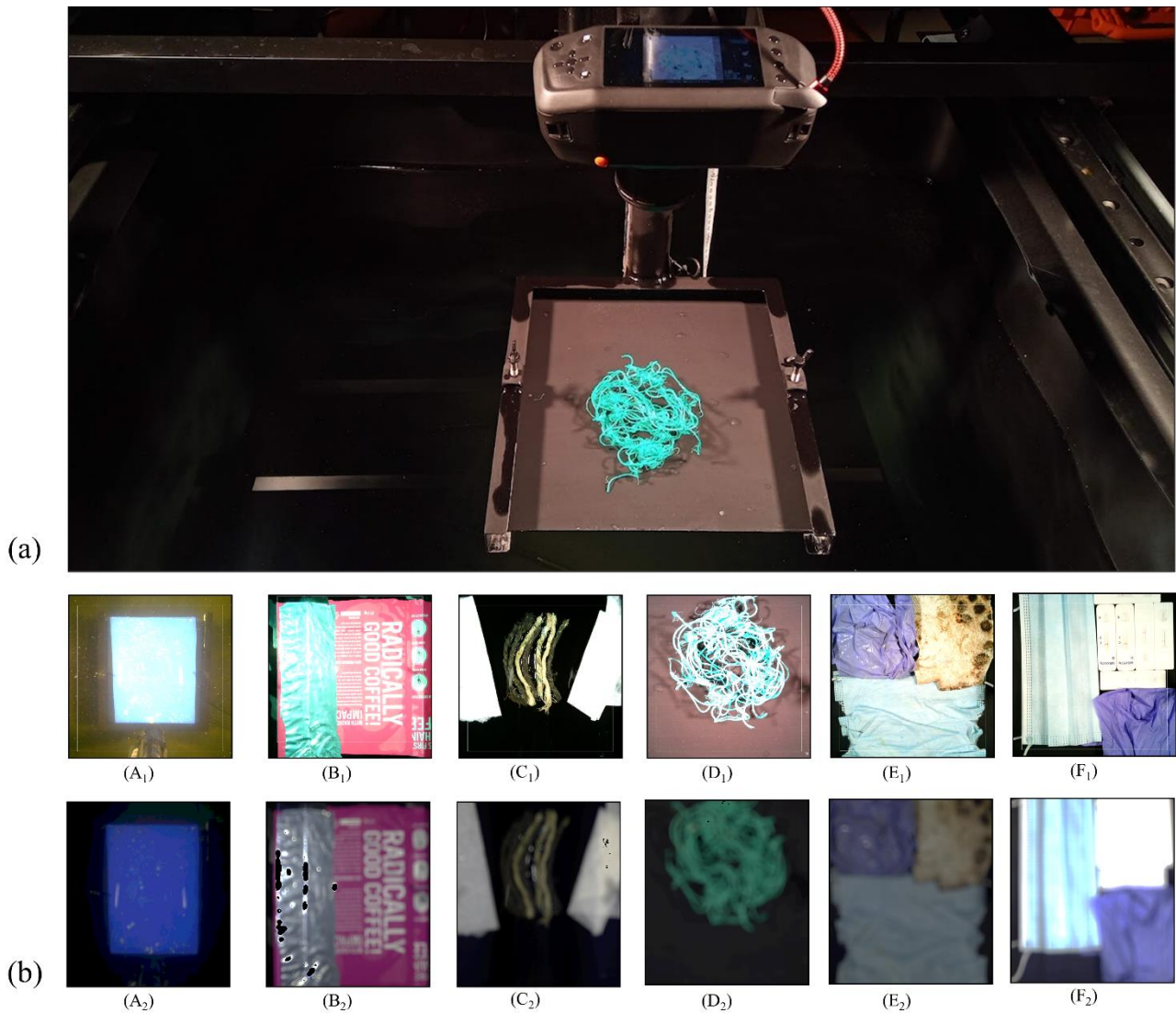
Figure 2 (a) The SPECIM IQ camera, positioned over one of the samples, and (b) the samples that were recorded by the SPECIM IQ. Subscript (1) denotes the image taken from the viewfinder, and subscript (2) denotes the RGB composite from the SPECIM hypercube. The
140 samples were: weathered ocean blue plastic front side (A), multilayer packaging, inside and outside combined (B), ocean rope (C), ocean green net (D), composite (old medical gloves, old medical face mask, white ocean plastic, (E)), and a composite of new face mask, new medical glove, and rapid antigen tests (F).

2.1.4 Sampling procedures

Observations involved taking a measurement starting with the dry samples followed by intervals of submersion to depth, then
145 finally just an above-water scenario of the wet target. The protocol was adopted from a prior study (Knaeps et al., 2021).

2.1.5 Processing, data structures, and analyses of measurements

Raw data files from spectral measurements were converted into a PostgreSQL 14 database. The data structure was generated to combine all essential metadata (Figure 3). Custom scripts in Python 3.8.8 with Matplotlib 3.3.4 and Pandas 1.2.4 libraries were used to visualize the data. No additional processing was applied to the data.
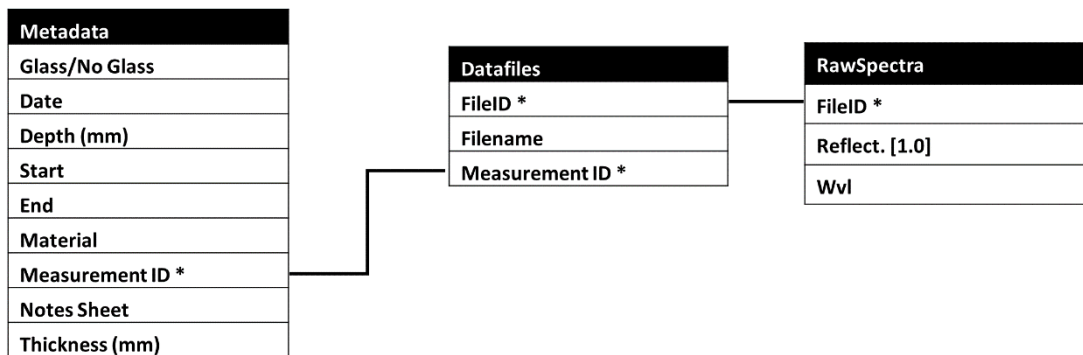
150

Figure 3 Data structure diagram for the hyperspectral measurement dataset. The table 'RawSpectra' contains the full set of raw data tables, concatenated from individual data files. The Metadata table contains the registration for each measurement and is linked to the RawSpectra through the Datafiles table. A Measurement ID from the Metadata table can have multiple FileIDS in the datafiles table. This also allows easy selection and aggregation of duplicate measurements for averaging and statistics.

155

2.2 Outdoors mesocosm campaign

2.2.1 Samples and biofouling

Biofouling is ubiquitous in all-natural aquatic environments, but replicating it is a challenging task that requires a delicate balance of environmental parameters. To understand how biofouling influences the detectability of plastics from remote sensing optical technologies, we conducted a long-term mesocosm experiment within a flow-through aquaculture system on the sub-tropical island of Oʻahu in Hawaiʻi, USA. The samples were pristine panels of HDPE, PP, PVC, PA6, PET-G, and XPS, similar to polymers described before (**Section 2.1.1**). The panels were kept submerged in seawater to allow the biofilm to grow for 88 days from 15 June to 11 September 2022 (**Figure 4**). During the incubation time, environmental parameters such as pH, chlorophyll-a (Chl-*a*), salinity, nitrates, and phosphates were monitored weekly while light properties (UVA, UVB, PAR), dissolved oxygen, seawater temperature, and air temperature were recorded at higher temporal resolutions (days to minutes).

After the incubation period of 88 days, the samples were carefully transported from the flow-through aquaculture system in containers filled with seawater to the study site. Since the measurement campaign took place at a different location and due to the fragility of the biofilm and quick disintegration and decomposition when left out of the water, the samples were submerged

in an adjacent seawater tidal canal to preserve the biofilm intact during the experiment. Each panel possessed a unique surface biofilm distribution (**Figure A2**).

| (a) | (b) | (c) | (d) | (e) |
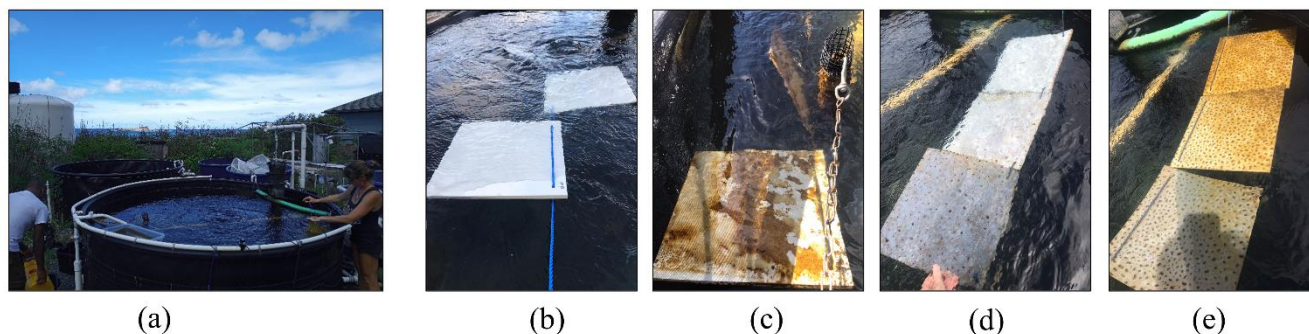
Figure 4 An overview of the biofouling tank (a); The sample biofouling process: (b) pristine samples are mounted in the tank, (c) the samples after a week of submersion, showing a biofilm which detached easily, (d) the bottom (tank-facing) of a sample set, after three months of biofouling, (e) the top (sky-facing) of the sample set, after three months of biofouling.

2.2.2   Experimental setup

A customized, cylindrical water tank was constructed and filled with fresh water. Using a seawater medium was considered but omitted, due to the lack of equipment to characterize the seawater at the measurement site. Hyperspectral point and multi-pixel measurements were conducted during daylight from 08:00 to 16:00 local time between 12 – 16 September 2022 on Oʻahu, Hawaiʻi, USA (**Figure 5**). The outdoor measurements of the samples at 0, 5, 50, and 250 mm water depth were completed using the SEV spectroradiometer. However, the degree of buoyancy and fragility of the 1 mm thick XPS sample did not allow submersion, and hence measurements were only conducted at the surface. The panels were fixated by a U-shaped bracket (**Figure 5a**). Before collecting the spectral measurements, water layer depth was recorded with a ruler (**Figure 5a, b**). The relative reflectance measurements were collected under natural light, and white referencing was performed with a SphereOptics Zenith Polymer® SG3120 ≈ 99 % full material PTFE standard panel before each measurement. During the campaign, the sky conditions ranged from cloudy to scattered clouds. Measurements were only collected when the conditions were stable (i.e. steady state cloud cover, or a steady window of clear sky). After the collection of all spectral reflectance measurements, the biofilm was carefully removed for further analysis (**Figure 5c**). The fore optic on the SEV was a 5° field-of-view lens and each measurement was an average of 20 scans (**Figure 5d**). The distance from the sensor to the water surface was 13 cm. The SPECIM IQ collected additional hypercube data of the biofouled samples at all water depths except above water (**Figure 5e**).
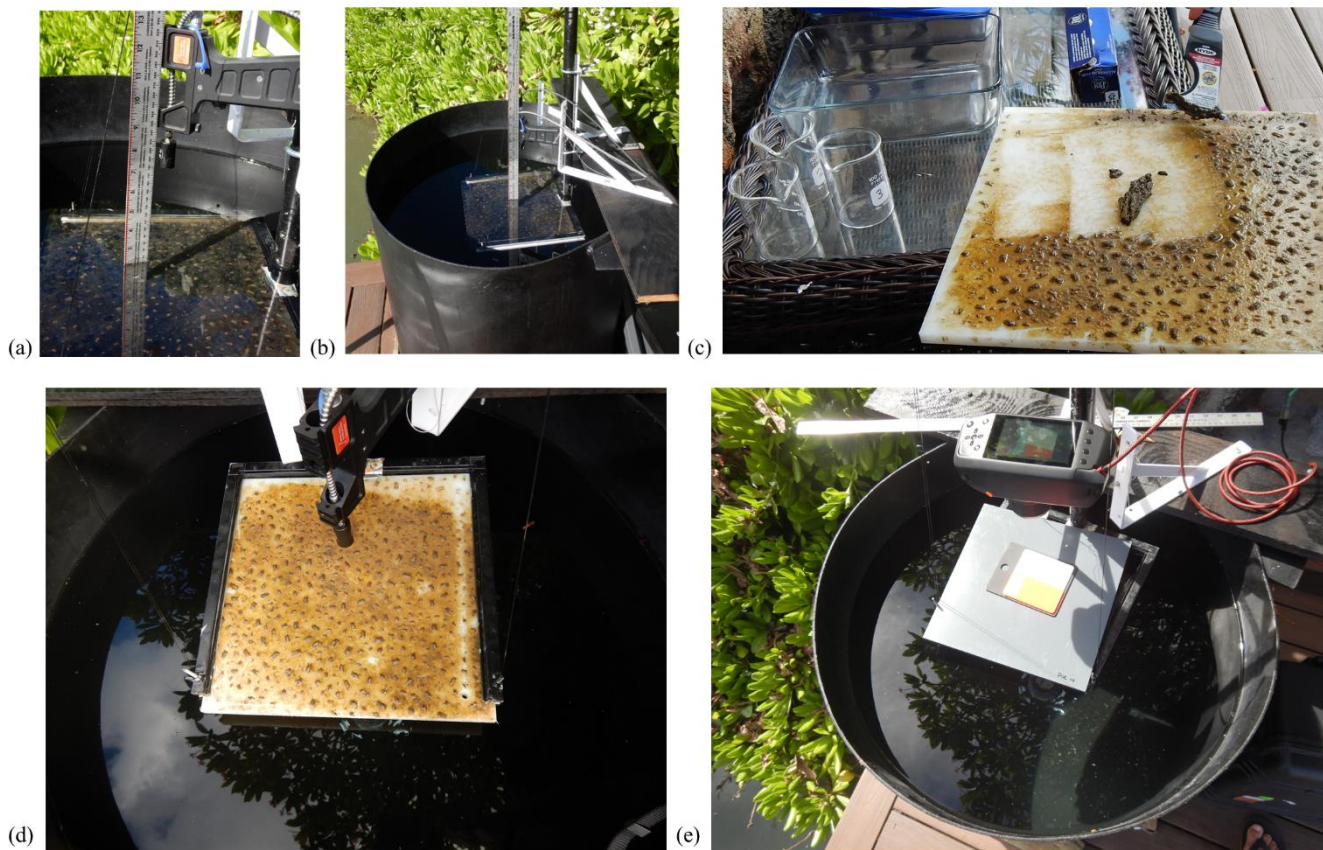
Figure 5 (a-b) Depth of submersion and distance of SEV lens to target measurements, (c) collection of biofilm to determine the biofilm mass for all the biofouled samples, (d) biofouled sample placed in position for SEV reflectance measurements and (e) SPECIM IQ camera collecting with a standard reference target.

2.2.3 Biofilm mass and thickness

A portable NiceGoodz electronic scale was used to determine the wet mass of the biofilm after removal from each panel (**Figure 5c**). Additionally, the thickness of the biofilm was estimated using a micrometer at three sample points. The pristine sample thickness was also recorded for reference against the manufacturer-reported thicknesses of the samples.

3   Results and discussion

3.1   SEV point measurements

3.1.1   Pristine samples (indoor campaign)

The spectral reflectance curves of the HDPE, PVC, PET-G, PA6, PP, and XPS panels with varying thicknesses and observed at depth are presented below (**Figure 6** and **Figure 8**), starting from a dry state just above the water surface (depth = 0 mm) and then followed by submerged observations. For more detail, **Figure 7** and **Figure 9** display the surface-level spectral reflectance of each material, including the confidence interval and individual measurement lines. In this section of the results and each of the following sections, each of the spectral reflectance curves is the average of a group of five measurements, unless mentioned otherwise. An increase in material thickness was revealed to cause an enhancement in the magnitude of detected reflectance for HDPE and PA6 but this was less pronounced in the other pristine plastics (**Figure 6** and **Figure 8**). It was also noted that for the thickest HDPE and PA6 samples, the inherent absorption features were enhanced in the near-surface water (0 – 50 mm) compared to thin samples. These PA6 and HDPE samples were semi-transparent which could influence these optical characteristics related to a direct correlation between thickness and signal magnitude. However, the fully transparent PET-G samples do not share the monotonic relationship between thickness and reflectance. Dark or transparent polymers tend to have a weak spectral reflectance even above water (e.g., XPS), which becomes weaker when submerged. Generally, the diagnostic absorption features appeared weak or relatively small in the SWIR for most thin plastics. This may have an impact on detectability in a noisy environment with other bright objects (i.e., with intense surface reflected glint, sea foam, breaking waves) or when the plastic pixel coverage is low.

We observed that the strong absorption of water in SWIR significantly affected the magnitude of reflectance measured for the pristine sampled with rapid loss of signal in the top layer (0 – 50 mm). From a first glance across all different polymer types, the SWIR (>1000 nm) part of the signal disappears beyond 50 mm water depth, while the visible domain (400 – 700 nm) remains present until the maximum depth of 70 cm. Even at 5 mm water depth, the spectral reflectance shape changes noticeably from the dry measurement for all polymer types investigated.
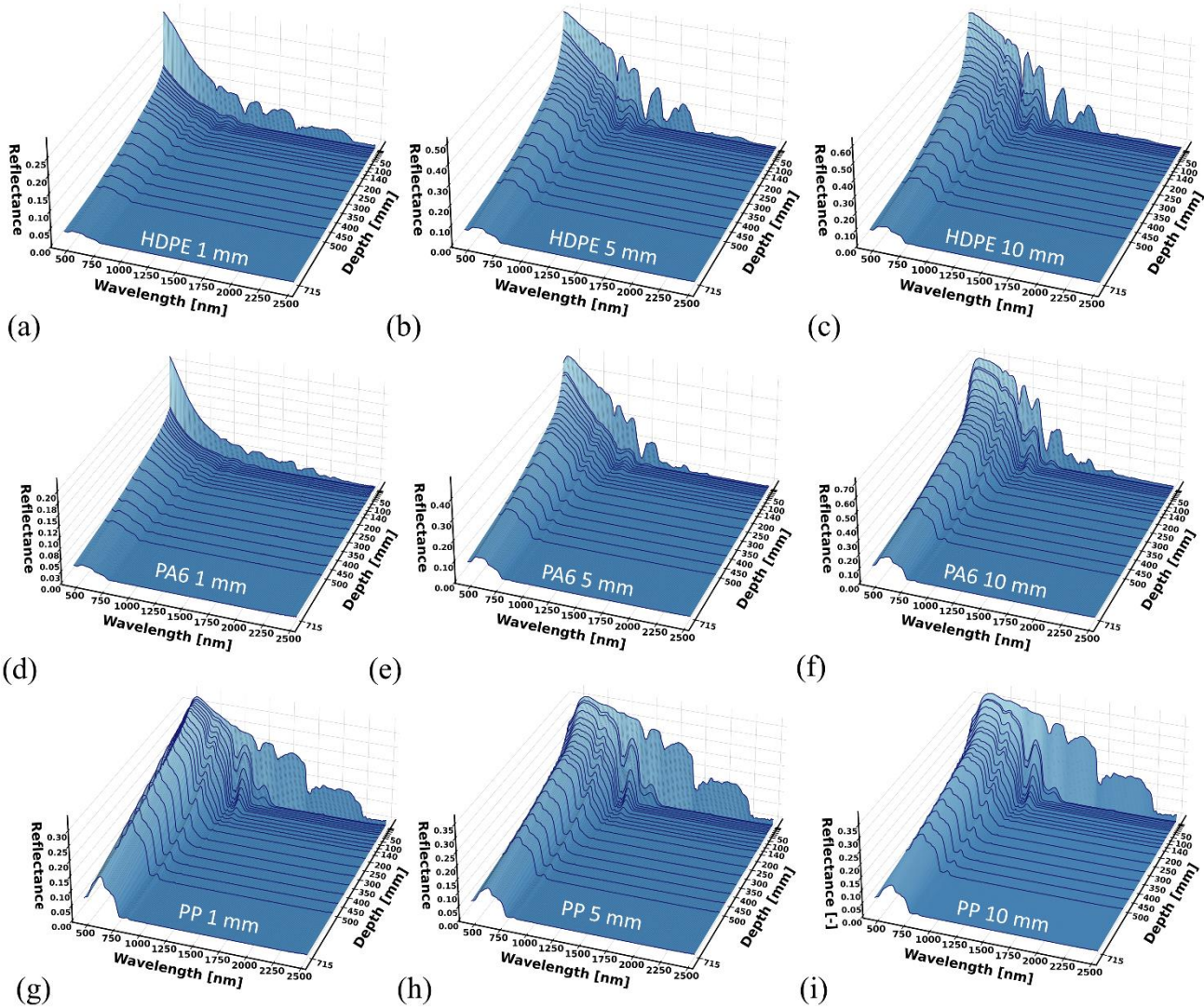
Figure 6 Spectral reflectance at varying depths for (a-c) HDPE, (d-f) PA6, and (g-i) PP for panel thickness ranging between 1 to 10 mm. Each reflectance curve is the average of five measurements.
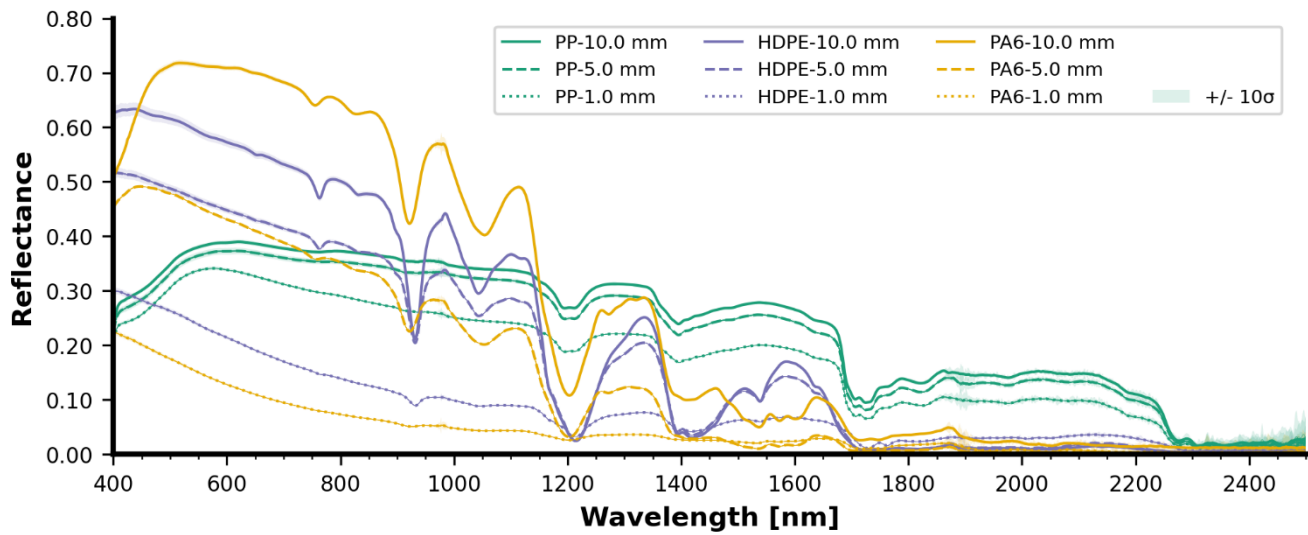
Figure 7 Surface-level spectral reflectance of the nine samples displayed in Figure 6. Each curve is accompanied by a 10σ confidence interval and individual measurement lines (hairlines), albeit barely visible due to the low variance of each set of five measurements.
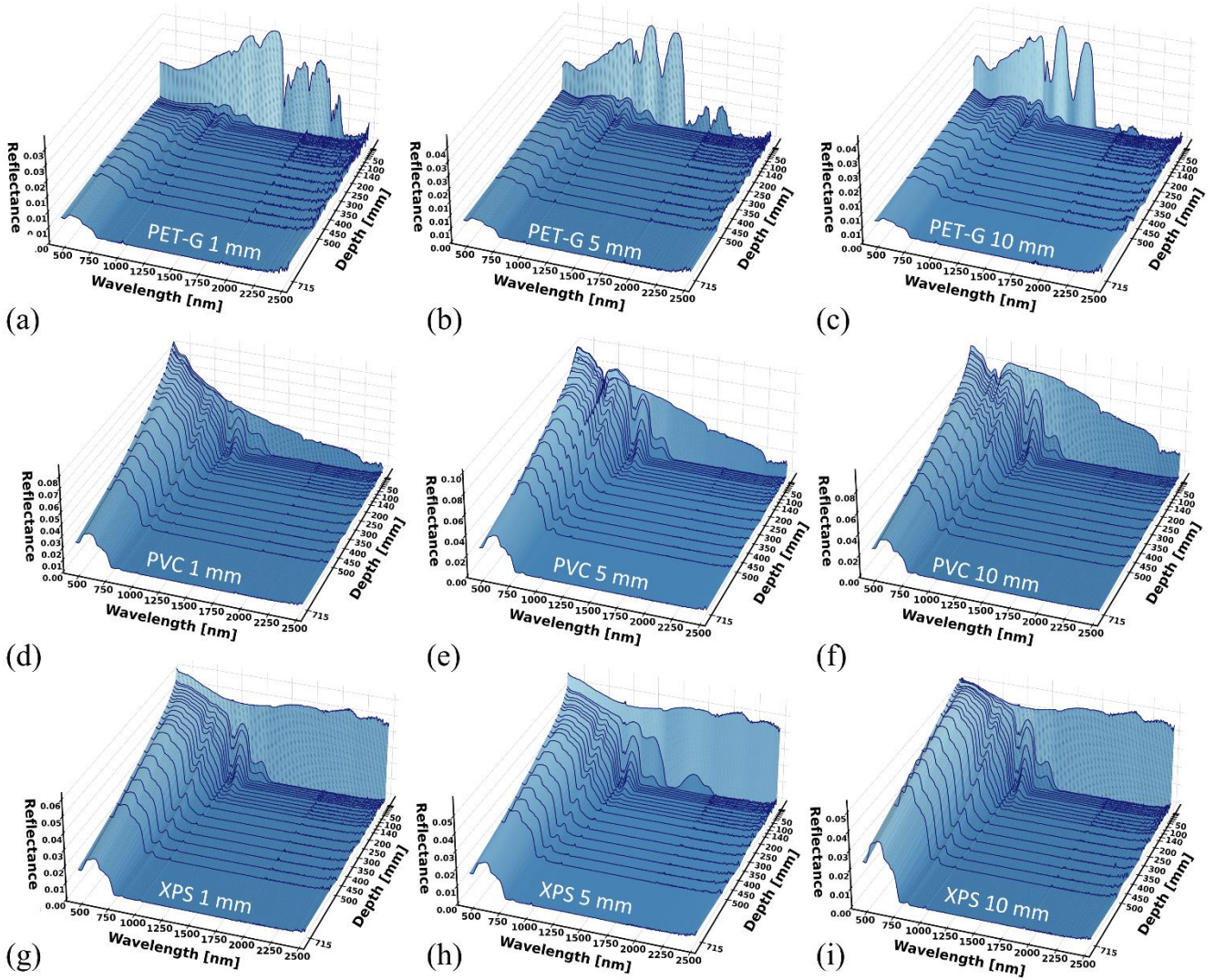
235 **Figure 8** Spectral reflectance at varying depths for (a-c) PET-G, (d-f) PVC, and (g-i) XPS for panel thickness ranging between 1 to 10 mm. Each reflectance curve is the average of five measurements.
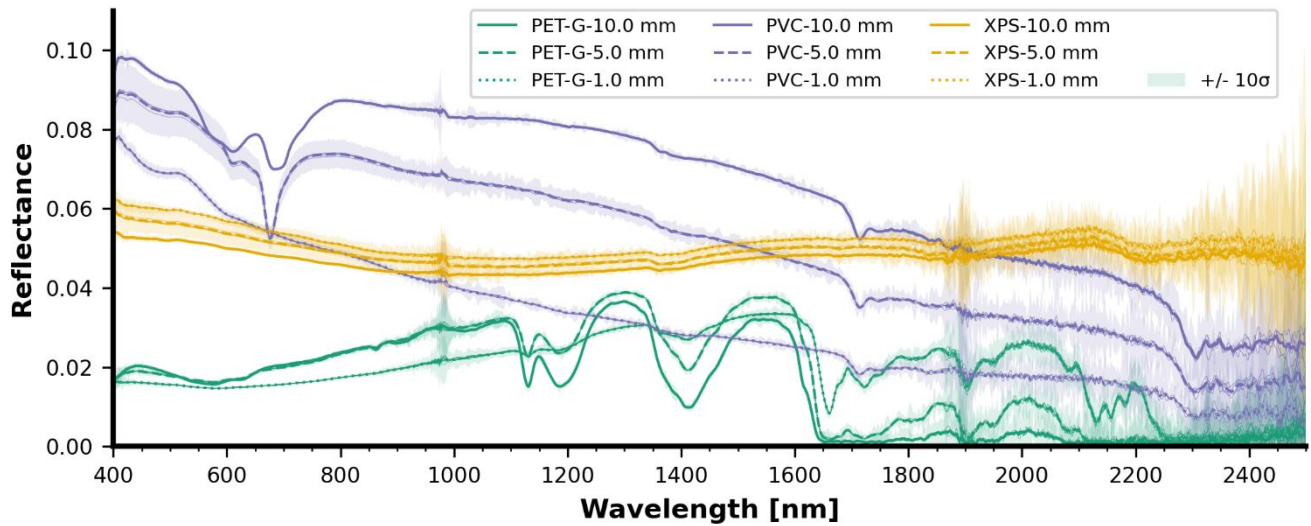
Figure 9 Surface-level spectral reflectance of the nine samples displayed in Figure 8. Each curve is accompanied by a 10σ confidence interval and individual measurement lines (hairlines).

240 **3.1.2   Construction materials, multilayer, and ocean-harvested, weathered plastics (indoor campaign)**

Weathered materials were also measured and these included multilayer packaging (both sides), blue weathered ocean plastic, white weathered ocean plastic, green ocean net, and weathered ocean rope. The spectral reflectance curves per depth are displayed in **Figure 10**. A special case appears in **Figure 10a** (inside of the multilayer sample): around 500 nm, the reflectance increases with depth, mostly between 200 and 500 mm depth. This effect could be caused by variations of the lighting and
245 viewing geometry with depth, combined with specular light reflection on the sample's aluminium coating. For extra detail, **Figure 11** displays the surface-level spectral reflectance of every material in **Figure 10**.
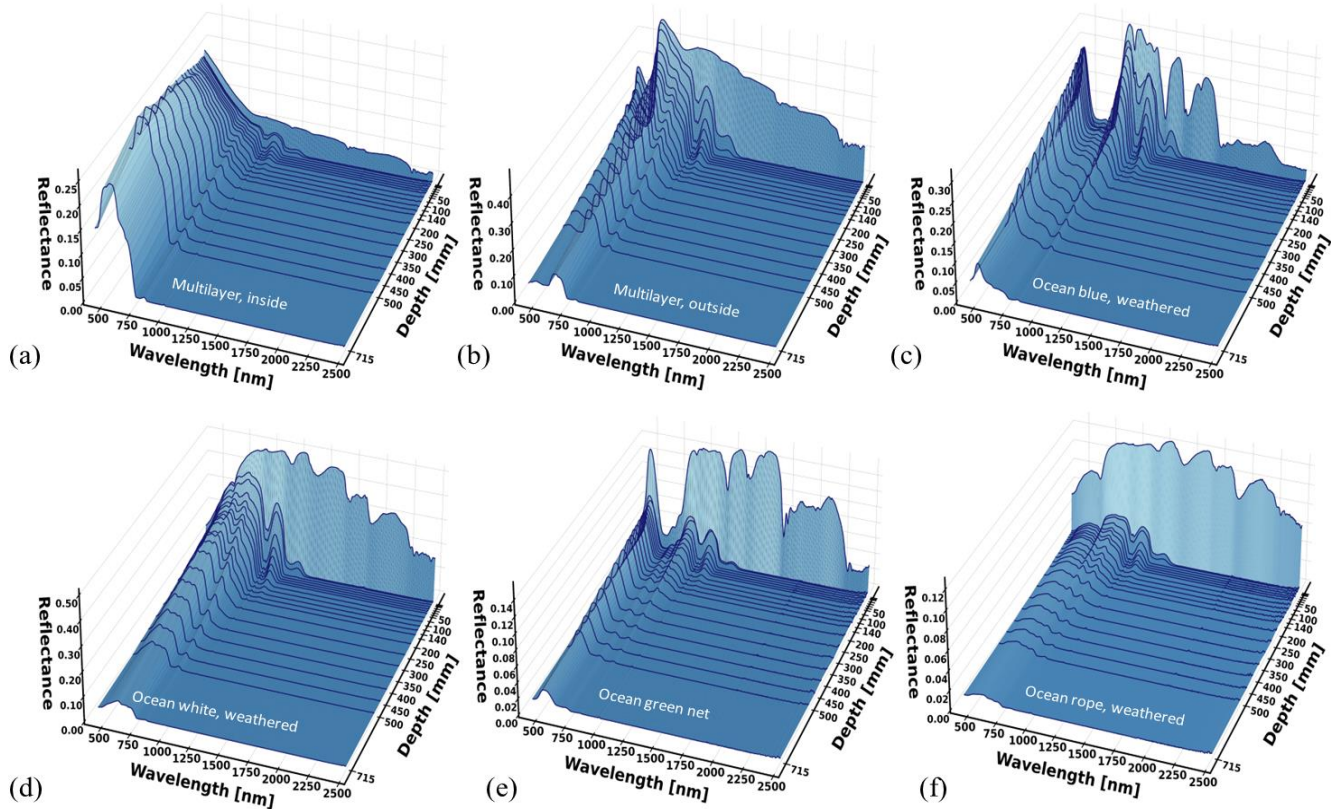
Figure 10 Spectral reflectance at varying depths for (a-b) multilayer inside and outside, (c) blue weathered ocean plastic,(d) white weathered biofouled dried ocean plastic, (e) a piece of green ocean net, and (f) weathered piece of ocean rope.
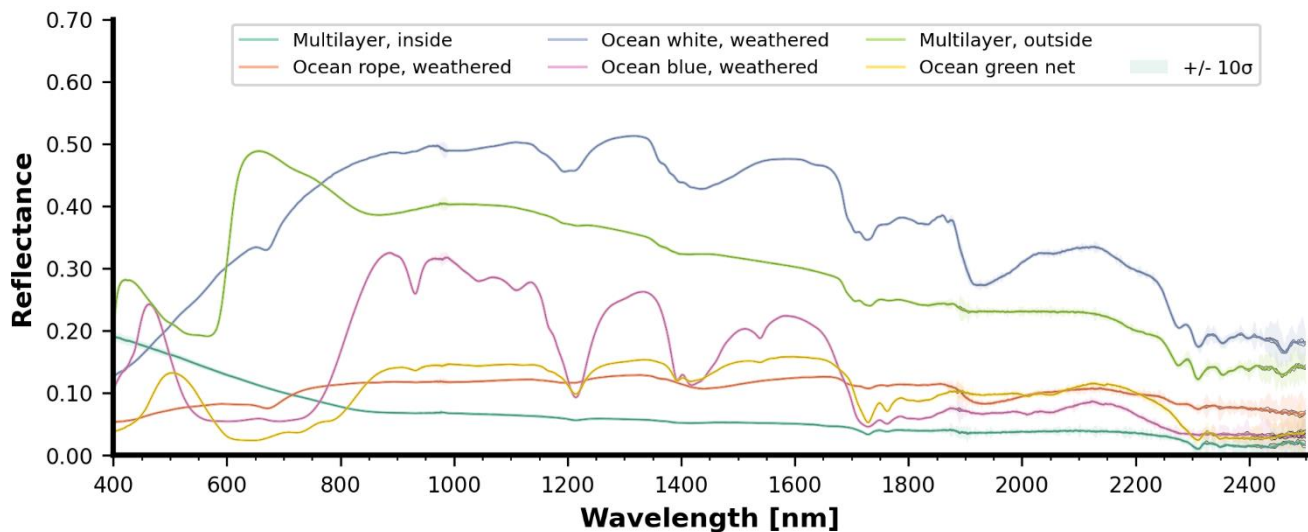
Figure 11 Surface-level spectral reflectance of the six materials displayed in Figure 10. Each curve is accompanied by a 10σ confidence interval and individual measurement lines (black hairlines), albeit barely visible due to the low variance of each set of five measurements.

255 Blue foam, white, brown, and green sail pieces (items 14 – 17 in **Table 2**) spectral reflectance measurements were only done in dry configuration **(see Figure 12** for the comparison of surface-level reflectance**)**. These weathered sailing pieces and a blue object were measured as representative items from nautical mismanaged waste. As can be seen in **Figure A1**, each sample of this group is large enough to fully cover the sensor pixel swath. Peaks in the visible spectrum matched the apparent colours e.g., blue foam (~450 nm) and green sail (~550 nm). The blue foam had the highest reflectance in the SWIR whilst the lowest

260 reflectance appears with the green sail. The overall reflectance magnitude differs between the materials and specifically in the NIR and SWIR, which could be explained by differences in material thickness (e.g. the sails being a film-like material versus the blue foam being a solid), as well as material brightness (e.g. the green sail being a darker material than the brown and white sail). The effect of material brightness, even in NIR and SWIR was also identified earlier in (Garaba et al., 2021).
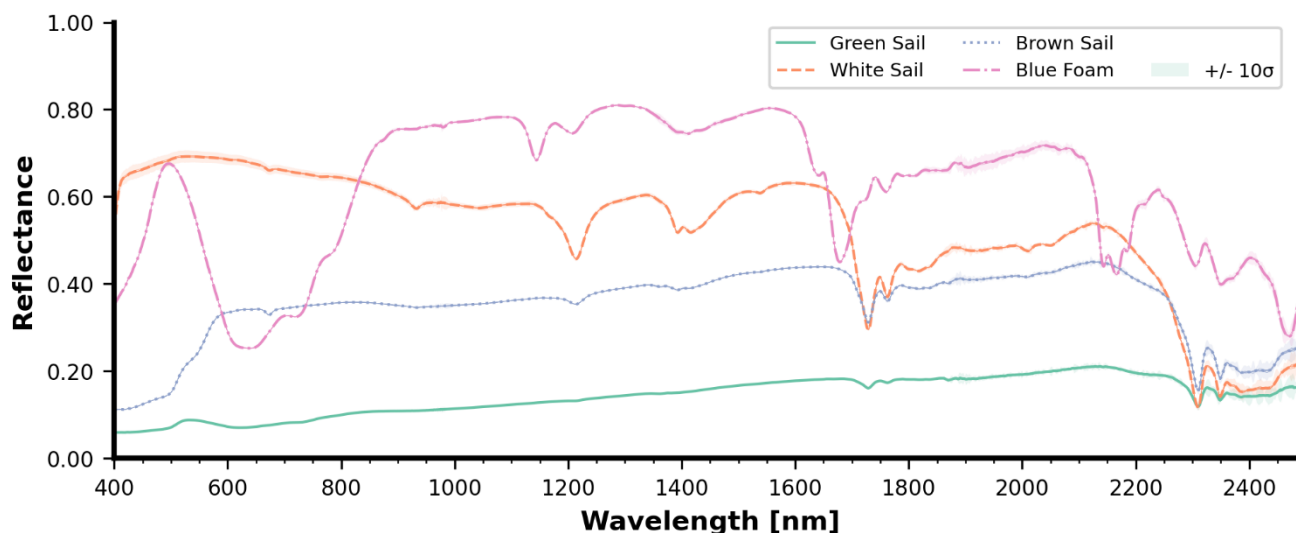
265 **Figure 12** Spectral reflectance of sailing-related objects, (a): white sail, sample ID 15 in Figure A1. (b): brown sail, sample ID 17 in Figure A1. (c): green sail, sample ID 16 in Figure A1. (d): blue foam, sample ID 14 in Figure A1. Each curve is accompanied by a 10σ confidence interval and individual measurement lines (colored hairlines), albeit barely visible due to the low variance of each set of five measurements.

3.1.3 (Indoor Campaign) COVID-19-related medical personal protective equipment (PPE)

Figure 13 presents an overview of the spectral reflectances for the different COVID-19-related PPE. Overall, the spectral

270 reflectance values of weathered facemasks and gloves are visibly lower than those of the new samples. An aged soaked medical glove has overall lower reflectance values than a dried, new glove. Above-water measurements of the facemasks (**Figure 13b**) were collected for both dry and soaked states. For the masks, soaking noticeably decreases reflectance values for wavelengths above 1200 nm. This effect becomes stronger when combined with the ageing of the samples. Soaking of the weathered facemask even before submersion almost completely negates spectral reflectance values in most of the SWIR bands. Most of

275 the remaining SWIR spectral reflectance is brought close to zero at 50 mm submersion depth. Finally, the measurements of

RAT tests (**Figure 13c**) that were only taken above the water surface, reveal a small difference in reflectance for the top and bottom faces. The RAT test spectral reflectance curves show absorption features around 1150 nm, 1250 nm, and 1650 nm.
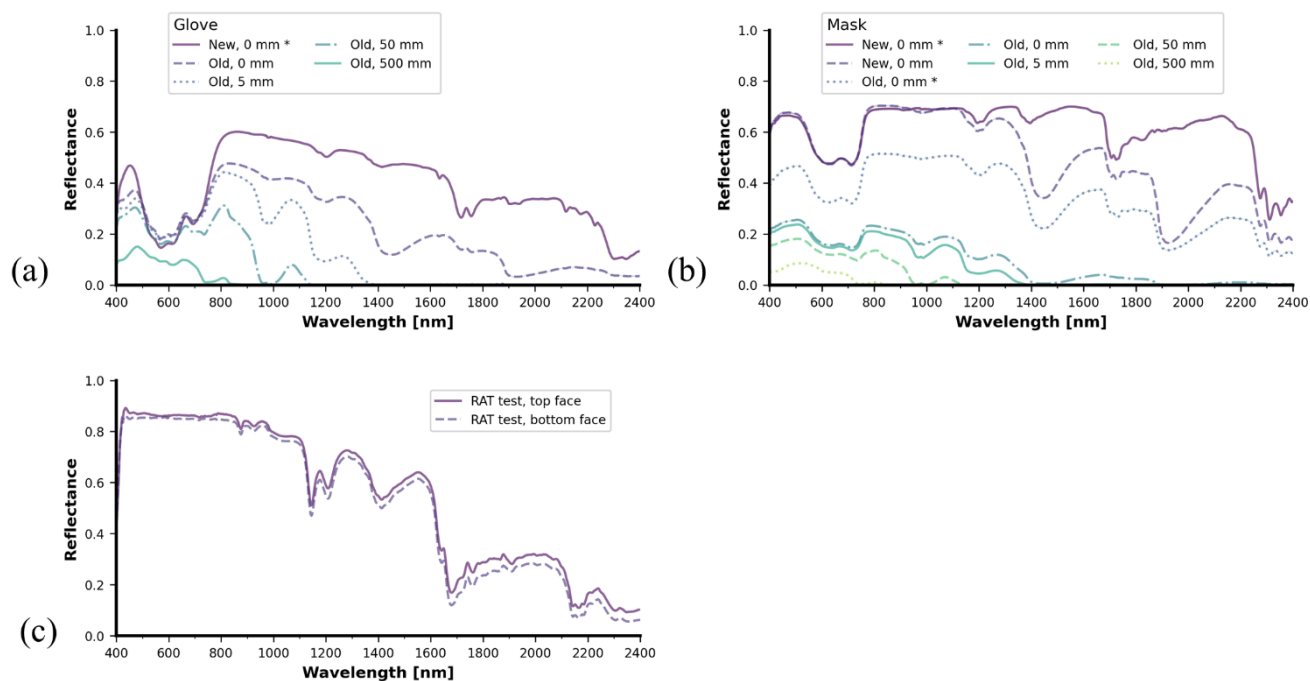
Figure 13 Spectral reflectance data from COVID-19-related medical waste in varying conditions: old and new surgical gloves from 0 to 500 mm depth (a), old and new medical masks from 0 to 500 mm depth (b), Rapid Antigen Tests (RAT)(c). For medical masks and gloves, the * denotes that a sample was dry or fully drained after submersion. Note that this study only examines one type of medical gloves and one type of medical mask, while medical PPE made of other types and materials also exists.

3.1.4   Blank measurements (indoor and outdoor)

For the indoor campaign, blank measurements were obtained by taking reflectance measurements with no sample in the sample holder. **Figure 14** shows the three types of indoor blank measurements: with only water, the sample holder plate without a glass window, and the sample holder plate with a glass window. The water alone shows negligible reflectance over the observed spectrum. The presence of the sample holder was noted to have a reflectance contribution of at most 0.05 in the infrared. Over most of the spectrum, the reflectance values of the sample holder with the glass window are lower than the reflectance values of the sample holder without the glass window. Blank measurements were also collected separately during the outdoor

290 mesocosm campaign. However, no holder plate was used. Therefore, the outdoor mesocosm blank measurements simplify to only the water background, which is also shown in **Figure 14**.
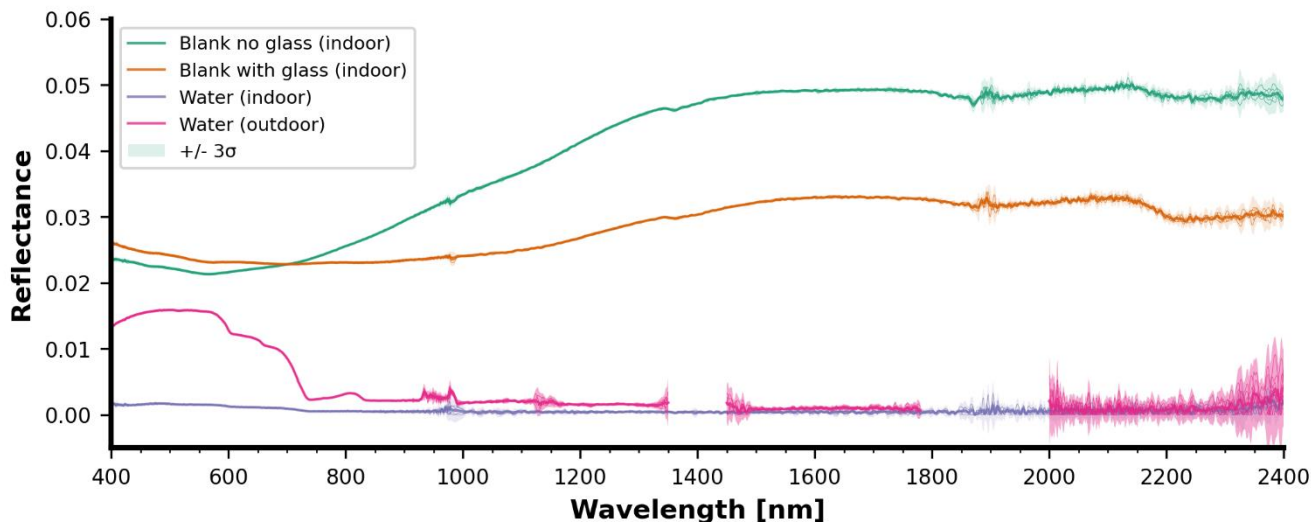
Figure 14 Comparison of different blank measurements above water, for both the indoor laboratory and the outdoor mesocosm campaign. All sample measurements during the indoor laboratory campaign were taken with the 'Glass' or 'No glass' option, depending on the required
295 setup. The black background plate has a higher reflectance than water. All measurements reported in this paper are raw measurements, meaning that the blank signal can still be subtracted to obtain material-specific reflectances with higher accuracy. Each curve is accompanied by a 3σ confidence interval and individual measurement lines (colored hairlines).

3.1.5   Biofouled samples (outdoor mesocosm)

The wet mass and thickness of the biofilm on the pristine samples exhibit a direct positive relationship (**Table 3**). Biofilm
300 thickness increased with sample thickness for HDPE, PP, and PA6. However, the variation of biofilm with substrate thickness seemed to be unclear for the other three polymers. The thickest and heaviest biofilm was found on the 10 mm HDPE samples.

Figure 15 compares the spectral reflectance of biofouled versus pristine samples for all the samples of 10 mm thickness. The shading around the lines indicates the standard deviation, obtained from the ensemble of 5 measurements. In the case of **Figure**
305 **15a**, variability of the sky cover influenced the 5 measurements belonging to the bioufouled measurement at 0 mm depth. This effect mainly impacts the reflectance magnitude but leaves the shape of the spectral reflectance curve unaltered. The same confidence intervals are also generated for the other subfigures but are nearly invisible due to very low signal variability during most of the measurements. The spectral reflectance shape in the SWIR (> 1000 nm) domain remains largely unchanged. In contrast, most of the impact occurs in the visible spectrum (400 – 700 nm). Although the biofilm thickness varied among the
310 different samples, this effect occurs for all samples, being most pronounced for HDPE (**Figure 15a**), PS (**Figure 15b**), and PA6 (**Figure 15f**). PET-G (**Figure 15c**) provides an exception in this case, as the biofouled sample was more reflective across the whole spectrum. Biofouled PP (**Figure 15d**) and PVC (**Figure 15e**) also both show a higher SWIR reflectance compared

to the pristine samples. By comparing with the 50 mm depth measurement, it becomes clear that water depth plays the strongest part in reflectance attenuation above 1000 nm. None of the samples had extremely thick biofouling. Biofilms in the GPGP are

315 expected to be even less significant in thickness and mass due to the oligotrophic marine environment in the open ocean. Yet, the biofilm grown on the samples in this study was relatively thick and representative of high-nutrient environments.

Table 3 Biofilm layer thicknesses and wet mass pristine plastic samples investigated between 12 – 16 September 2022 in Honolulu, Hawaiʻi, USA.

Polymer type	Polymer thickness (mm)	Mean pristine thickness (mm)	Biofilm thickness (mm)	Mean wet biofilm mass (g)
HDPE	10	9.84	2.24	22.60
	5	5.11	0.97	17.40
	1	1.20	0.09	4.27
PP	10	10.08	0.47	9.60
	5	5.09	0.35	2.43
	1	1.06	0.16	0.40
PS	10	9.91	0.73	2.00
	5	5.07	0.25	0.97
	1	0.83	0.12	1.17
PET-G	10	9.97	1.19	2.50
	5	4.86	0.25	1.40
	1	1.02	0.20	2.77
PVC	10	10.00	0.11	4.03
	5	4.88	0.20	3.93
	1	1.09	0.31	4.03
PA6	10	11.45	0.96	7.10
	5	5.25	0.77	3.80
	1	1.00	0.29	5.00
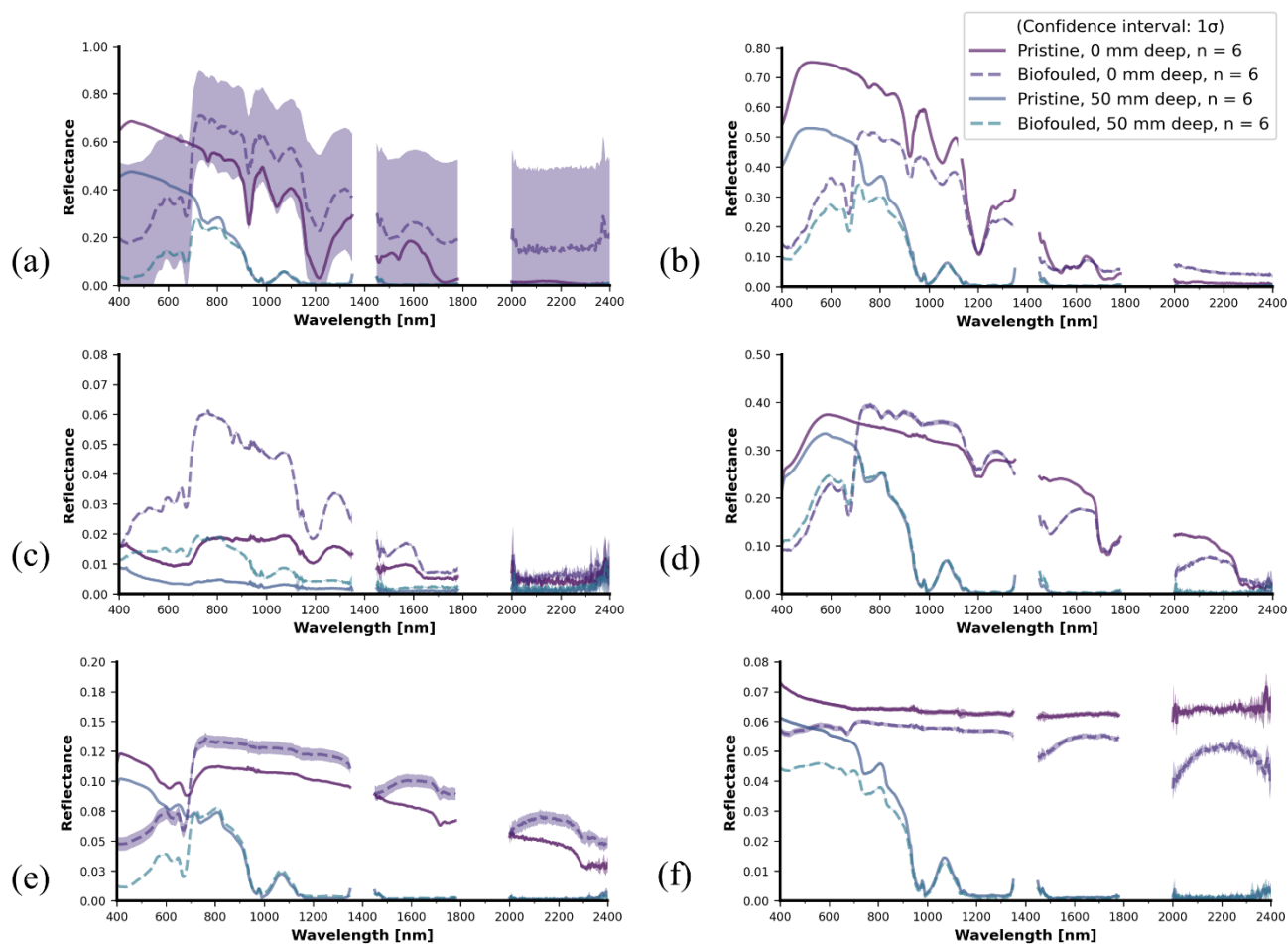
Figure 15 (a) 10 mm thickness HDPE, pristine and biofouled. The main difference occurs in the visible spectrum (400 – 700 nm), which is relatively dark. The biofilm does not obscure any of the typical spectral features; **(b)** 10 mm thickness PA6, pristine and biofouled. Here, the biofilm generally decreases the spectral reflectance magnitude, with the strongest diminishing effect in the visible (400 – 700) spectrum. Nevertheless, the spectral reflectance shape beyond 700 nm changes minimally; **(c)** 10 mm thickness PET-G, pristine and biofouled. The reflectance magnitude increases considerably across the entire spectrum for the biofouled sample compared to the pristine sample; **(d)** 10 mm thickness PP, pristine and biofouled. The main difference occurs in the visible spectrum (400 – 700 nm), which is relatively dark. Spectral features are not influenced by the biofilm; **(e)** 10 mm thickness PVC, pristine and biofouled. The biofilm mostly decreases the spectral reflectance magnitude in the visible (400 – 700 nm) spectrum. The spectral reflectance shape beyond 700 nm changes minimally; **(f)** 10 mm thickness XPS, pristine and biofouled. Only minimal differences occur, mainly in the < 700 nm part of the spectrum.

3.2 Specim IQ hypercubes (indoor campaign)

Figure 16 presents an example of several spectra obtained from the Specim IQ hypercube data: the dark background (A), a medical facemask (B), a medical glove (C), the marine-harvested and weathered white PP plastic (D), and the biofouled PP sample (E). The displayed reflectance curves are obtained by averaging the data from ten points on each sample. Between the curves, we can distinguish the relatively high reflectance of the biofouled PP sample. Because the SPECIM IQ range is limited

to 400 – 1000 nm no information could be derived about the SWIR diagnostic features. Yet, the SPECIM IQ data is unique

335   and offers the potential to further examine spatial heterogeneity of spectral reflectance on irregular samples. **Figure 16** also includes the mean and standard deviation of each sample, each obtained from an ensemble of 10 points extracted from the sample hypercube.

When comparing **Figure 16** with the point measurements data in **Figure 11** (weathered white plastic), **Figure 13** (medical PPE), and **Figure 15d** (biofouled HDPE), the spectral reflectance magnitudes are different. Observing the spread in individual

340   measurement lines in **Figure 16**, the difference in reflectance magnitudes is likely caused by differences in sampling location. The SPECIM IQ reflectance curves are based on the mean of a point ensemble, while a SEV point measurement is based on the average of the sensor pixel swath.
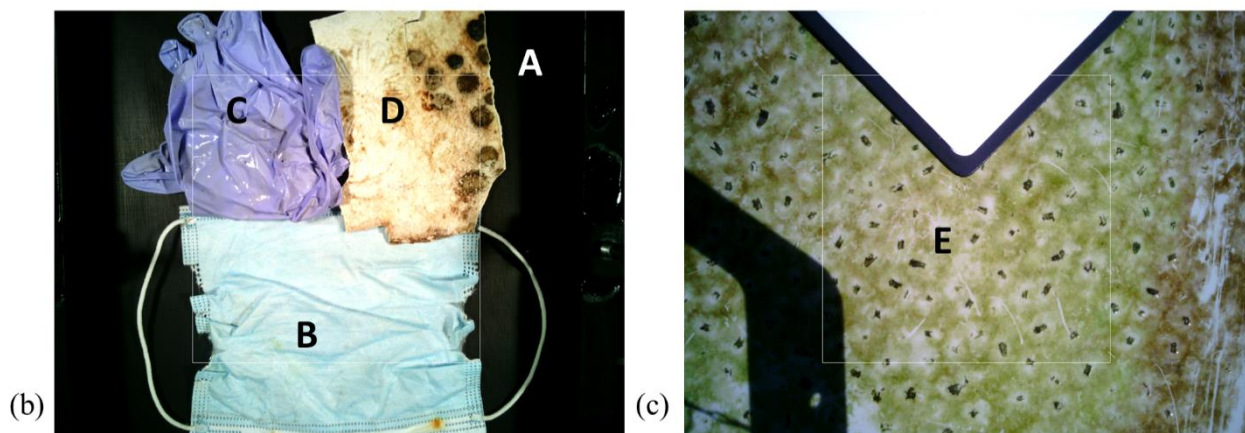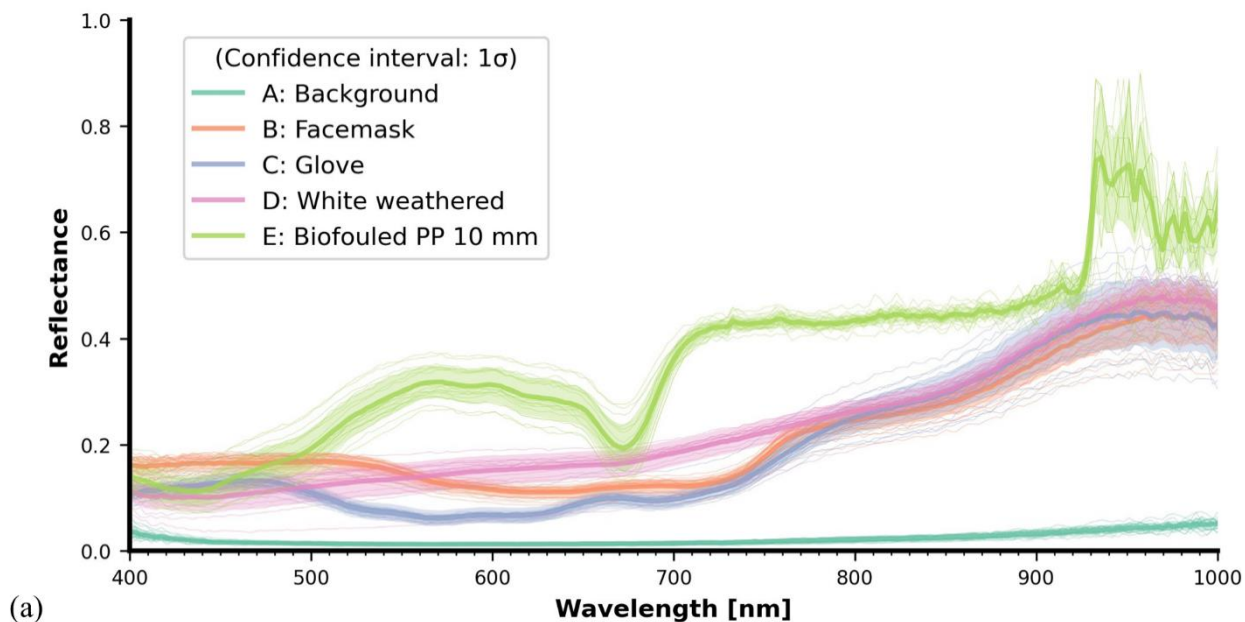
Figure 16 (a) Example spectra, aggregated from the SPECIM IQ hypercube data. For each of the spectral reflectance curves, at least ten points were sampled from the hypercube. The confidence intervals are obtained as the standard deviation of the data points across each sample. (b) The multi-material sample is represented by curves A, B, C, D. (c) Additional 10 mm thickness biofouled PP sample, represented by curve E. . Each curve is accompanied by a 1σ confidence interval and individual measurement lines (colored hairlines).

4   Data availability

The indoor laboratory data are available in open access through https://doi.org/10.4121/769cc482-b104-4927-a94b-b16f6618c3b3 (de Vries and Garaba, 2023). The outdoor experiment involving the biofouling samples is available at https://doi.org/10.4121/7c53b72a-be97-478b-9288-ff9c850de64b (de Vries et al., 2023).

5   Conclusions

This study presents and describes an open-access spectral reflectance dataset that was collected in an indoor and outdoor laboratory setting. This dataset provides an opportunity for the scientific community to further examine the relation between submersion in the water column, material properties, biofouling, and key diagnostic wavelengths for plastic marine litter.

Additionally, the data visualizations conducted here have already prompted several observations: Firstly, water depth has a strong influence on the spectral reflectance, as expected. Several diagnostic wavelengths in the SWIR spectrum become obscured at shallow (50 mm) water depths. Secondly, the material thickness influences the magnitude and contrast of spectral reflectance for several polymer types. The relation between material thickness and reflectance was strongest for HDPE and PA6. Finally, biofouling had a mixed effect on the spectral reflectance magnitude, depending on the material type and wavelength. However, the biofilm did not impact the shape of the spectral reflectance curve significantly in the SWIR. Water depth and material thickness appeared to remain the most significant factors for the spectral reflectance of floating and submerged plastic marine litter.

From a wider perspective and in comparison with recent comparable studies, the dataset presented in this study brings additional detail and range to the domain of hyperspectral remote sensing of plastic marine litter, by including COVID-19-related samples, ocean-harvested samples from the GPGP, live microcosm measurements and imaging. Furthermore, the inclusion of standardized pristine plastic samples is expected to increase comparability with other studies that have used the same standardized sample set. The hypercube scans of the heterogeneous samples are intended to further enrich the dataset, by enabling inspection of the spectral effects of spatial heterogeneity in material ageing and biofouling.

Appendix A
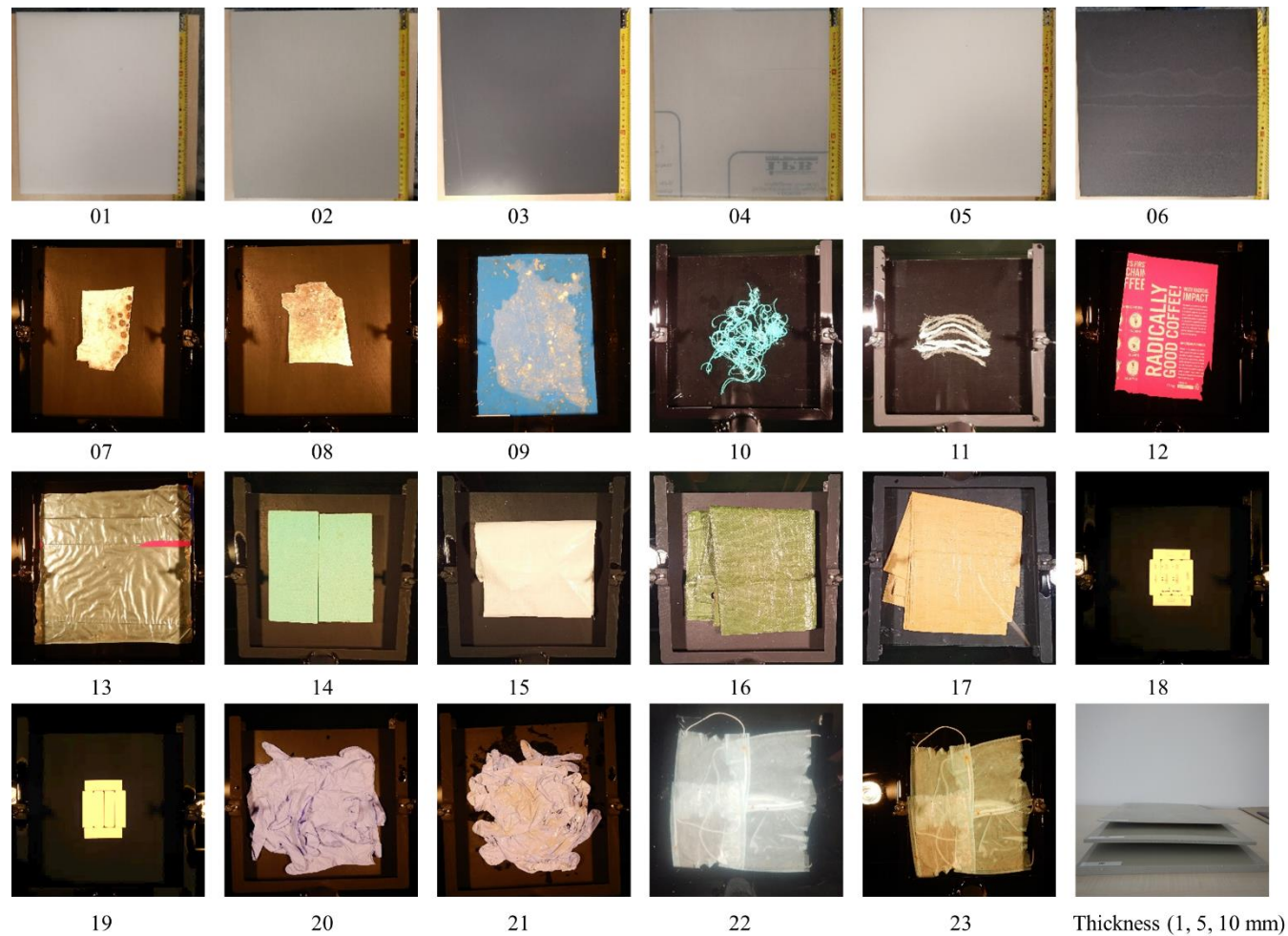
Figure A1 Overview photos of the sampled pristine (01 – 06) and weathered (07 - 23) plastics observed in August/September 2021 during the reflectance measurement campaign.
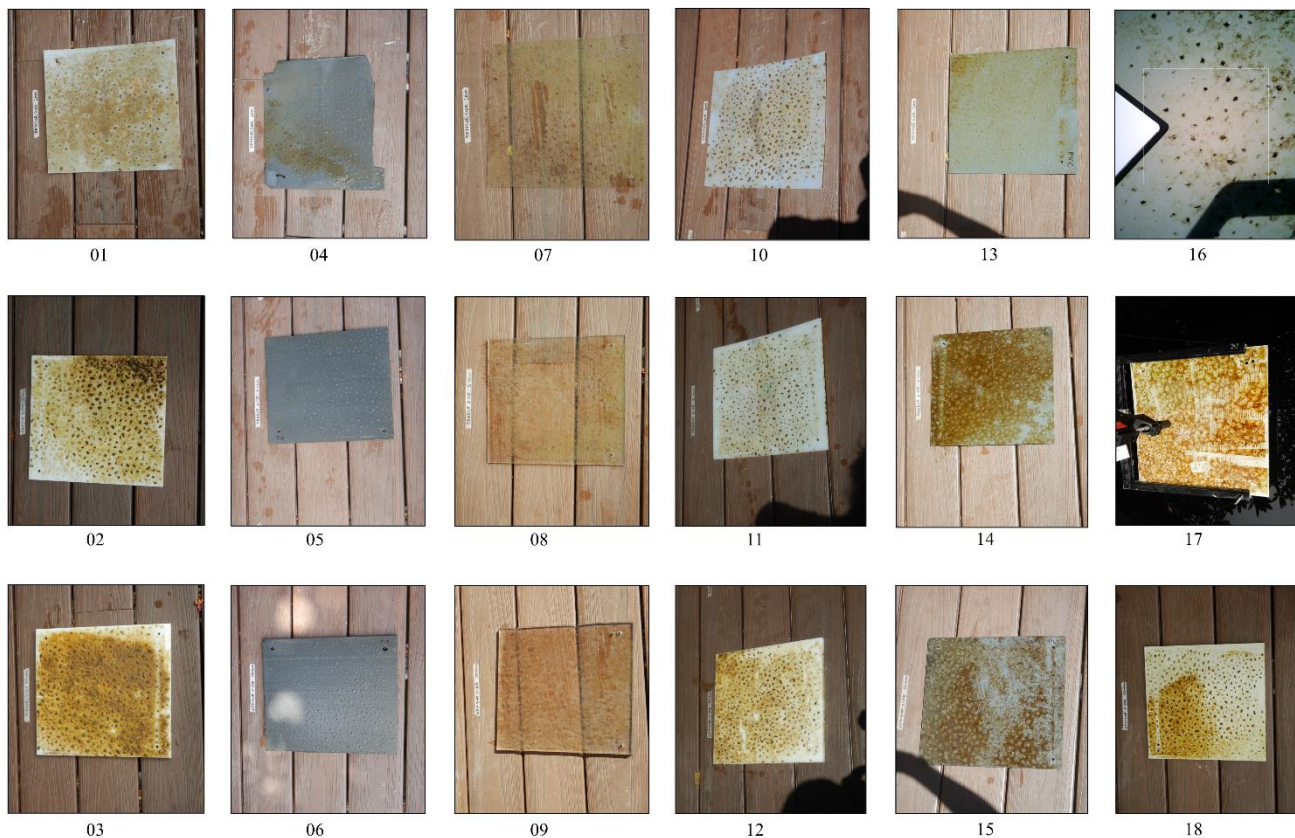
380

Figure A2 Overview of biofouled samples, used in the outdoor measurement campaign: HDPE (01 - 03), XPS (04-06), PET-G (07-09), PA6 (10-12), PVC (13-15), PP (16-18). Rosws from top to bottom denote 1, 5, and 10 mm thickness, respectively. For PP 1 mm (16), the viewfinder preview of the SPECIM IQ camera is used as the overview image was found missing.

Appendix B

Figure B1 displays the time series data of the environmental variables during the biofouling microcosm: air temperature, UV irradiance, PAR density, and seawater temperature.
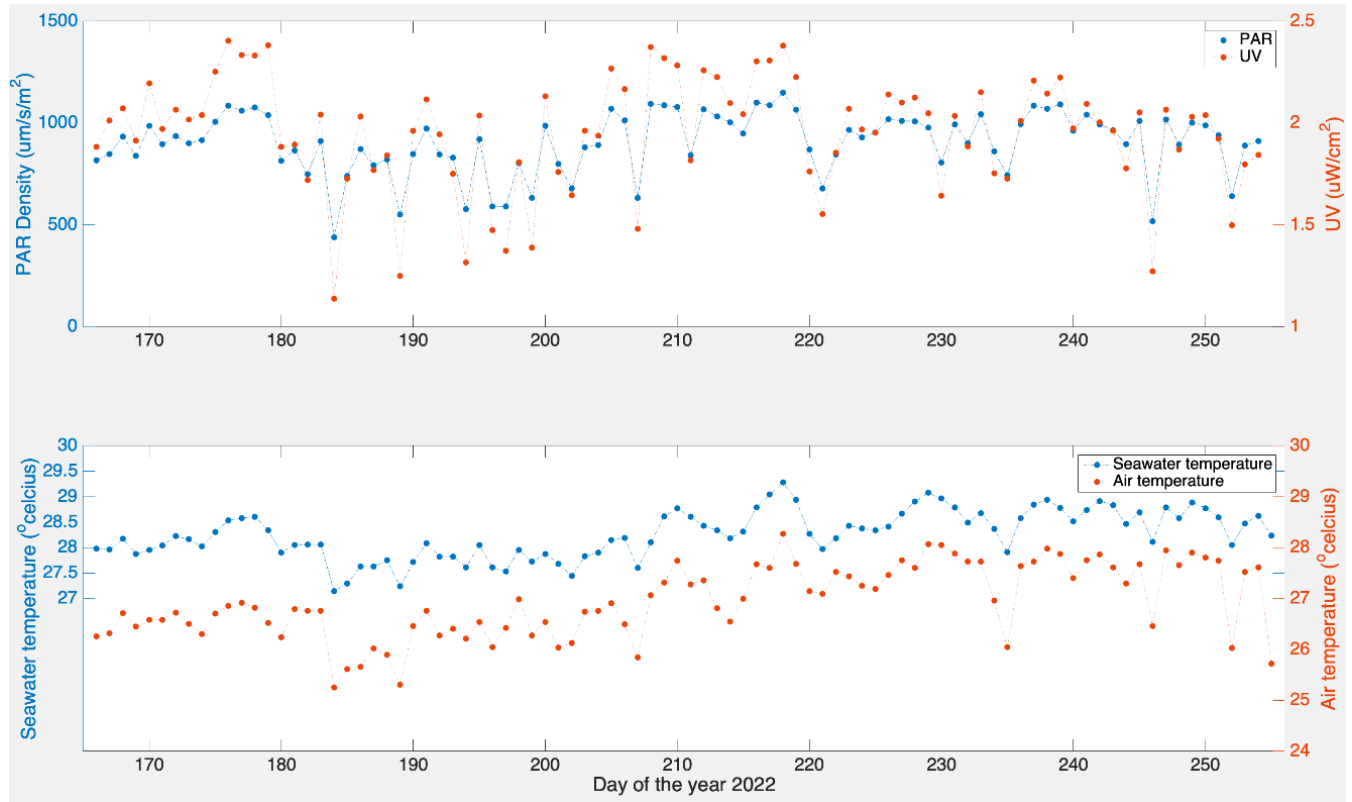
Figure B1 Daily average of the ultraviolet radiation (UV), photosynthetically active radiation (PAR), seawater, and air temperature measurements (°C) of the microcosm experiment from 15 June to 11 September 2022 during local daytime from sunrise to sunset.

Appendix C

Table C1: Detailed characteristics of the biofilm on the biofouling microcosm experiment.

Polymer type	Polymer thickness (mm)	Thicknesses (no biofilm) (mm)			Mean thickness (mm)	Std thickness (mm)	Thicknesses (with biofilm) (mm)			Mean thickness (mm)	Std thickness (mm)	Biofilm thickness (mm)	Weight (wet biofilm) (g)			Mean weight (mm)	Std weight (mm)	Weight (wet biofilm) (g) FACE DOWN
HDPE	10	9.81	9.61	10.1	9.84	0.25	12.19	12.26	11.80	12.08	0.25	2.24	22.5	22.7	22.6	22.60	0.10	1
	5	5.01	5.14	5.18	5.11	0.09	5.94	6.86	5.45	6.08	0.72	0.97	17.3	17.6	17.3	17.40	0.17	1.1
	1	1.3	1.28	1.03	1.20	0.15	1.36	1.32	1.21	1.30	0.08	0.09	4.2	4.6	4	4.27	0.31	1
PP	10	10.05	10.23	9.96	10.08	0.14	10.40	10.77	10.49	10.55	0.19	0.47	9.6	9.5	9.7	9.60	0.10	1.5
	5	5.09	5.12	5.06	5.09	0.03	5.24	5.70	5.37	5.44	0.24	0.35	2.5	2.4	2.4	2.43	0.06	1.1
	1	1.06	1.06	1.07	1.06	0.01	1.16	1.19	1.32	1.22	0.09	0.16	0.4	0.5	0.3	0.40	0.10	0.1
PS	10	9.92	9.95	9.85	9.91	0.05	10.12	10.85	10.95	10.64	0.45	0.73	2.1	1.9	2	2.00	0.10	0
	5	5.02	5.09	5.1	5.07	0.04	5.16	5.48	5.33	5.32	0.16	0.25	1.1	0.8	1	0.97	0.15	0
	1	0.86	0.8	0.83	0.83	0.03	1.02	0.91	0.93	0.95	0.06	0.12	1	1.1	1.4	1.17	0.21	0
PET-G	10	10.01	9.96	9.94	9.97	0.04	11.11	11.58	10.79	11.16	0.40	1.19	2.5	2.4	2.6	2.50	0.10	2
	5	4.83	4.88	4.87	4.86	0.03	5.04	5.09	5.19	5.11	0.08	0.25	1.4	1.5	1.3	1.40	0.10	1.1
	1	1.02	1.03	1.01	1.02	0.01	1.17	1.20	1.30	1.22	0.07	0.20	2.8	2.8	2.7	2.77	0.06	0.8
PVC	10	9.98	10.01	10.02	10.00	0.02	10.14	10.09	10.10	10.11	0.03	0.11	4	4.1	4	4.03	0.06	3.2
	5	4.87	4.9	4.88	4.88	0.02	5.08	5.01	5.16	5.08	0.08	0.20	3.9	3.9	4	3.93	0.06	3.1
	1	1.1	1.07	1.1	1.09	0.02	1.42	1.46	1.33	1.40	0.07	0.31	4	4.1	4	4.03	0.06	1.1
PA6	10	11.52	11.41	11.43	11.45	0.06	12.48	12.44	12.32	12.41	0.08	0.96	7.1	7.2	7	7.10	0.10	2.8
	5	5.24	5.22	5.28	5.25	0.03	5.96	6.00	6.10	6.02	0.07	0.77	3.8	3.7	3.9	3.80	0.10	1.4
	1	1	1.01	1	1.00	0.01	1.24	1.31	1.34	1.30	0.05	0.29	5.1	4.9	5	5.00	0.10	1.5

395

Appendix D
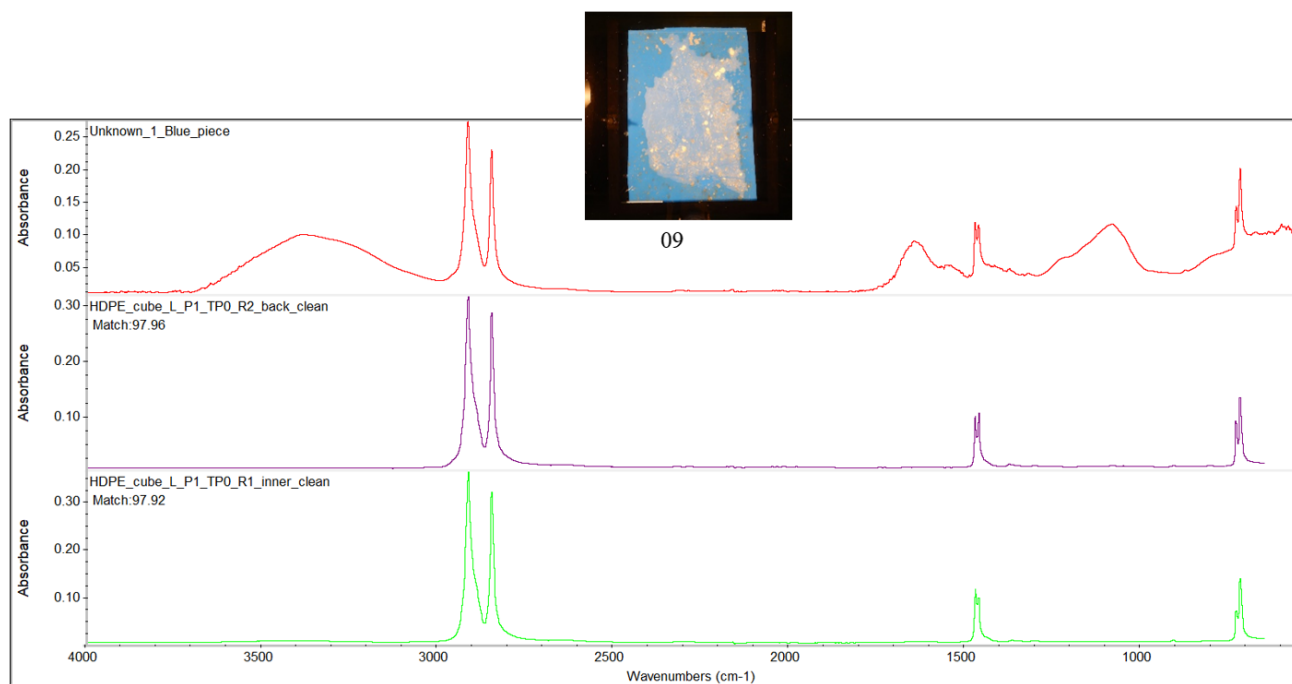
Figure D1 FTIR spectrum of the blue ocean-harvested plastic, indicating a match with HDPE.

400
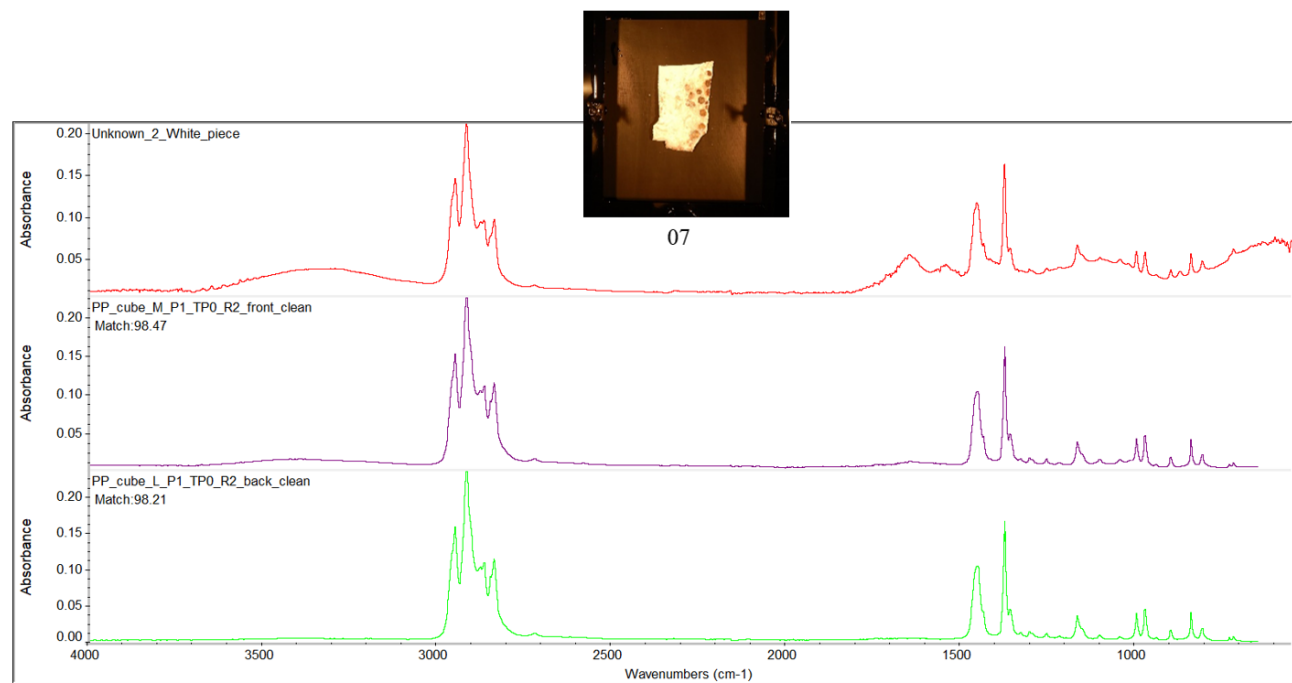
Figure D2 FTIR spectrum of the ocean-harvested white piece of plastic, indicating a match with PP.
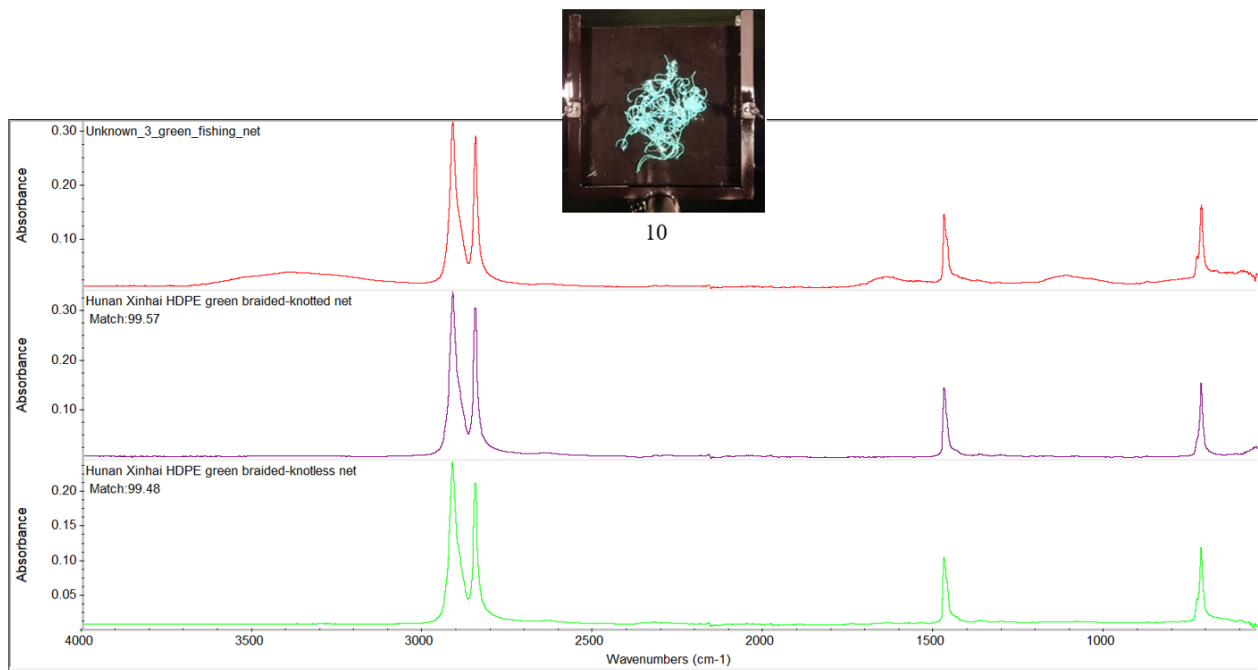
Figure D3 FTIR spectrum of the ocean-harvested green fishing net sample, indicating a match with HDPE.

405

Acknowledgments

We are grateful for the Wilhelmshaven tank construction by Gerrit Behrens, Helmo Nicolai, and Waldemar Siewert. We also
410 thank Timo Sanders for the sample preparation, and Steon Engineering Plastics for supplying the pristine plastics. We thank
the Hawai'i Pacific University and the Center for Marine Debris Research for hosting the biofouling microcosm in their
facilities. We thank Paolo Corradi of the European Space Agency for discussions about the study, and we wish to acknowledge
the Discovery Element of the European Space Agency's Basic Activities for the funding of this work. Finally, we thank The
Ocean Cleanup's donors, as the ocean-harvested samples and biofouling setup in Hawaii would not have been possible without
415 them.

Author contribution

RdV, SPG, and S-JR designed the experimental setup and conducted the data collection and preparation. RdV performed
project management, data quality control, data visualization, and preparation of the dataset for open access. All authors
discussed and approved the manuscript text.

420 **Competing interests**

The authors declare that they have no conflict of interest.

Financial support

Funding for this work was from the Discovery Element of the European Space Agency's Basic Activities (ESA contract no.
4000132036/20/NL/GLC and 4000132037/20/NL/ GLC). SPG was also supported by the Deutsche Forschungsgemeinschaft
425 grant no. 417276871.

References

Barboza, L. G. A., Dick Vethaak, A., Lavorante, B. R. B. O., Lundebye, A.-K., and Guilhermino, L.: Marine microplastic
debris: An emerging issue for food security, food safety and human health, Mar. Pollut. Bull., 133, 336–348,
430 https://doi.org/doi:10.1016/j.marpolbul.2018.05.047, 2018.
Beaumont, N. J., Aanesen, M., Austen, M. C., Börger, T., Clark, J. R., Cole, M., Hooper, T., Lindeque, P. K., Pascoe, C., and
Wyles, K. J.: Global ecological, social and economic impacts of marine plastic, Mar. Pollut. Bull., 142, 189–195,
https://doi.org/10.1016/j.marpolbul.2019.03.022, 2019.

Benson, N. U., Bassey, D. E., and Palanisami, T.: COVID pollution: impact of COVID-19 pandemic on global plastic waste

435 footprint., Heliyon, 7, e06343, https://doi.org/10.1016/j.heliyon.2021.e06343, 2021.

Garaba, S. P. and Dierssen, H. M.: Hyperspectral ultraviolet to shortwave infrared characteristics of marine-harvested, washed-ashore and virgin plastics, Earth Syst. Sci. Data, 12, 77–86, https://doi.org/10.5194/essd-12-77-2020, 2020.

Garaba, S. P. and Harmel, T.: Top-of-atmosphere hyper and multispectral signatures of submerged plastic litter with changing water clarity and depth, Opt. Express, 30, 16553, https://doi.org/10.1364/oe.451415, 2022.

440 Garaba, S. P., Aitken, J., Slat, B., Dierssen, H. M., Lebreton, L., Zielinski, O., and Reisser, J.: Sensing Ocean Plastics with an Airborne Hyperspectral Shortwave Infrared Imager, Environ. Sci. Technol., https://doi.org/10.1021/acs.est.8b02855, 2018.

Garaba, S. P., Acuña-Ruz, T., and Mattar, C. B.: Hyperspectral longwave infrared reflectance spectra of naturally dried algae, anthropogenic plastics, sands and shells, Earth Syst. Sci. Data, 12, 2665–2678, https://doi.org/10.5194/essd-12-2665-2020, 2020.

445 Garaba, S. P., Arias, M., Corradi, P., Harmel, T., de Vries, R., and Lebreton, L.: Concentration, anisotropic and apparent colour effects on optical reflectance properties of virgin and ocean-harvested plastics, J. Hazard. Mater., 406, 124290, https://doi.org/10.1016/j.jhazmat.2020.124290, 2021.

GESAMP: Guidelines for the monitoring and assessment of plastic litter in the ocean, Rep. Stud. GESAMP, no 99, 130p, 2019.

450 Goddijn-Murphy, L. and Dufaur, J.: Proof of concept for a model of light reflectance of plastics floating on natural waters., Mar. Pollut. Bull., 135, 1145–1157, https://doi.org/10.1016/j.marpolbul.2018.08.044, 2018.

Guffogg, J. A., Blades, S. M., Soto-Berelov, M., Bellman, C. J., Skidmore, A. K., and Jones, S. D.: Quantifying marine plastic debris in a beach environment using spectral analysis, Remote Sens., 13, 1–23, https://doi.org/10.3390/rs13224548, 2021.

Knaeps, E., Sterckx, S., Strackx, G., Mijnendonckx, J., Moshtaghi, M., Garaba, S. P., and Meire, D.: Hyperspectral-reflectance

455 dataset of dry, wet and submerged marine litter, Earth Syst. Sci. Data, 13, 713–730, https://doi.org/10.5194/essd-13-713-2021, 2021.

Kooi, M., Reisser, J., Slat, B., Ferrari, F. F., Schmid, M. S., Cunsolo, S., Brambini, R., Noble, K., Sirks, L. A., Linders, T. E. W., Schoeneich-Argent, R. I., and Koelmans, A. A.: The effect of particle properties on the depth profile of buoyant plastics in the ocean, Sci. Rep., 6, 1–10, https://doi.org/10.1038/srep33882, 2016.

460 Law, K. L., Morét-Ferguson, S. E., Goodwin, D. S., Zettler, E. R., DeForce, E., Kukulka, T., and Proskurowski, G.: Distribution of Surface Plastic Debris in the Eastern Pacific Ocean from an 11-Year Data Set, Environ. Sci. Technol., 48, 4732–4738, https://doi.org/10.1021/es4053076, 2014.

Lebreton, L., Slat, B., Ferrari, F., Aitken, J., Marthouse, R., Hajbane, S., Sainte-Rose, B., Aitken, J., Marthouse, R., Hajbane, S., Cunsolo, S., Schwarz, A., Levivier, A., Noble, K., Debeljak, P., Maral, H., Schoeneich-Argent, R., Brambini, R., and

465 Reisser, J.: Evidence that the Great Pacific Garbage Patch is rapidly accumulating plastic, Sci. Rep., 8, 1–15, https://doi.org/10.1038/s41598-018-22939-w, 2018.

Leone, G., Catarino, A. I., De Keukelaere, L., Bossaer, M., Knaeps, E., and Everaert, G.: Hyperspectral reflectance dataset of

pristine, weathered, and biofouled plastics, Earth Syst. Sci. Data, 15, 745–752, https://doi.org/10.5194/essd-15-745-2023, 2023.

470   Martínez-Vicente, V., Clark, J. R., Corradi, P., Aliani, S., Arias, M., Bochow, M., Bonnery, G., Cole, M., Cózar, A., Donnelly, R., Echevarría, F., Galgani, F., Garaba, S. P., Goddijn-Murphy, L., Lebreton, L., Leslie, H. A., Lindeque, P. K., Maximenko, N., Martin-Lauzer, F.-R., Moller, D., Murphy, P., Palombi, L., Raimondi, V., Reisser, J., Romero, L., Simis, S. G. H., Sterckx, S., Thompson, R. C., Topouzelis, K. N., van Sebille, E., Veiga, J. M., and Vethaak, A. D.: Measuring marine plastic debris from space: Initial assessment of observation requirements, Remote Sens., 11, 2443, https://doi.org/doi:10.3390/rs11202443,

475   2019.

Maximenko, N., Corradi, P., Law, K. L., Sebille, E. Van, Garaba, S. P., Lampitt, R. S., Galgani, F., Martinez-Vicente, V., Goddijn-Murphy, L., Veiga, J. M., Thompson, R. C., Maes, C., Moller, D., Löscher, C. R., Addamo, A. M., Lamson, M. R., Centurioni, L. R., Posth, N. R., Lumpkin, R., Vinci, M., Martins, A. M., Pieper, C. D., Isobe, A., Hanke, G., Edwards, M., Chubarenko, I. P., Rodriguez, E., Aliani, S., Arias, M., Asner, G. P., Brosich, A., Carlton, J. T., Chao, Y., Cook, A.-M., Cundy,

480   A. B., Galloway, T. S., Giorgetti, A., Goni, G. J., Guichoux, Y., Haram, L. E., Hardesty, B. D., Holdsworth, N., Lebreton, L., Leslie, H. A., Macadam-Somer, I., Mace, T., Manuel, M., Marsh, R., Martinez, E., Mayor, D. J., Moigne, M. Le, Jack, M. E. M., Mowlem, M. C., Obbard, R. W., Pabortsava, K., Robberson, B., Rotaru, A.-E., Ruiz, G. M., Spedicato, M. T., Thiel, M., Turra, A., and Wilcox, C.: Toward the Integrated Marine Debris Observing System, Front. Mar. Sci., 6, https://doi.org/10.3389/fmars.2019.00447, 2019.

485   Park, Y.-J., Garaba, S. P., and Sainte-Rose, B.: Detecting the Great Pacific Garbage Patch floating plastic litter using WorldView-3 satellite imagery, Opt. Express, 29, 35288, https://doi.org/10.1364/oe.440380, 2021.

Van Sebille, E., Aliani, S., Law, K. L., Maximenko, N., Alsina, J. M., Bagaev, A., Bergmann, M., Chapron, B., Chubarenko, I., Cózar, A., Delandmeter, P., Egger, M., Fox-Kemper, B., Garaba, S. P., Goddijn-Murphy, L., Hardesty, B. D., Hoffman, M. J., Isobe, A., Jongedijk, C. E., Kaandorp, M. L. A., Khatmullina, L., Koelmans, A. A., Kukulka, T., Laufkötter, C., Lebreton,

490   L., Lobelle, D., Maes, C., Martinez-Vicente, V., Morales Maqueda, M. A., Poulain-Zarcos, M., Rodríguez, E., Ryan, P. G., Shanks, A. L., Shim, W. J., Suaria, G., Thiel, M., Van Den Bremer, T. S., and Wichmann, D.: The physical oceanography of the transport of floating marine debris, Environ. Res. Lett., 15, https://doi.org/10.1088/1748-9326/ab6d7d, 2020.

Tasseron, P., van Emmerik, T., Peller, J., Schreyers, L., and Biermann, L.: Advancing Floating Macroplastic Detection from Space Using Experimental Hyperspectral Imagery, Remote Sens., 13, 2335, https://doi.org/10.3390/rs13122335, 2021a.

495   Tasseron, P., van Emmerik, T., Schreyers, L., Biermann, L., and Peller, J.: Hyperspectral plastics dataset supplementary to the paper 'Advancing floating plastic detection from space using hyperspectral imagery,' https://doi.org/10.4121/14518278.v3, 2021b.

Topouzelis, K., Papakonstantinou, A., and Garaba, S. P.: Detection of floating plastics from satellite and unmanned aerial systems (Plastic Litter Project 2018), Int. J. Appl. Earth Obs. Geoinf., 79, 175–183, https://doi.org/10.1016/j.jag.2019.03.011,

500   2019.

United Nations Environment Programme: From pollution to solution: A global assessment of marine litter and plastic pollution,

Nairobi, 148 pp., 2021.

de Vries, R., Egger, M., Mani, T., and Lebreton, L.: Quantifying Floating Plastic Debris At Sea Using Vessel-Based Optical Data and Artificial Intelligence, Int. Geosci. Remote Sens. Symp., 1118–1121, https://doi.org/10.1109/IGARSS47720.2021.9554154, 2021.

de Vries, R. V. F. and Garaba, S. P.: Dataset of spectral reflectances and hypercubes of submerged plastic litter, including COVID-19 medical waste, pristine plastics, and ocean-harvested plastics, https://doi.org/10.4121/769cc482-b104-4927-a94b-b16f6618c3b3.v1, 2023.

de Vries, R. V. F., Garaba, S. P., and Royer, S.-J.: Dataset of spectral reflectances and hypercubes of submerged biofouled, pristine, and ocean-harvested marine litter, https://doi.org/10.4121/7c53b72a-be97-478b-9288-ff9c850de64b.v1, 2023.